# Alcothermal and Nitrilethermal Synthesis of Metal Oxides Nanomaterials and Their Applications

Meiliefiana

1248007

A dissertation submitted to the

Engineering course, Department of Engineering,

Graduate School of Engineering,

Kochi University of Technology,

Kochi, Japan

in partial fulfillment of the requirements for the degree of

Doctor of Engineering

Assessment Committee:

Supervisor: Professor Kazuya Kobiro

Co-supervisor: Professor Nagatoshi Nishiwaki

Co-supervisor: Professor Masataka Ohtani

Associate Professor Akitaka Ito

Professor Hisao Makino

September, 2023

# Abstract

Metal oxides have attracted much attention owing to their intrinsic properties of thermal stability, abundant oxygen vacancies, and huge specific surface area. Furthermore, the combination of several metal oxides as mixed metal oxides assemblies in nanoscale known as nano-composites offers an opportunity to enhance the properties of metal oxides for wide applications, including heterogeneous catalysts, catalyst supports, and sensor materials. However, composites suffer from poor stability if they are placed in harsh conditions, such as high-temperatures, particularly in catalyst and catalyst support applications. Embedded metal nanoparticles (NPs) in the pores of base metal oxides are one of the most effective approach to improve catalyst stabilities. In general, embedded metal NPs into metal oxides suppress the sintering phenomenon of metal NPs at high temperatures by physical separation of the metal NPs. Porous metal oxides have been used as catalyst supports for the embedded metal NPs because of their large surface area and high porosity. In this context, a new strategy to embed metal NPs in porous catalyst supports has been developed. To clarify this strategy, Ni nanoparticle catalysts embedded in $ZrO_2$ porous spheres and $ZrO_2$ porous composite spheres such as $SiO_2$–$ZrO_2$, MgO–$ZrO_2$, and $Y_2O_3$–$ZrO_2$ were synthesized by one-pot single-step alcothermal method. The obtained Ni catalysts have high specific surface areas of 130–196 $m^2/g$ even after high-temperature $H_2$ reduction at 450 °C for 2 h. They were utilized as catalysts for low-temperature dry reforming of methane (DRM) at 550 °C and effectively suppressed carbon deposition on Ni nanoparticles embedded in $SiO_2$–$ZrO_2$ and $Y_2O_3$–$ZrO_2$.

Moreover, performance and stability of supported metal catalysts also strongly depend on the inherent properties of the supports, on which the metals are dispersed. The

properties of catalyst support can be controlled by modifying the synthetic conditions. To interpret this concept, $CeO_2$ porous spheres and their composites were synthesized by modified simple one-pot and single-step solvothermal method using acetonitrile as a solvent, which was termed “nitrilethermal” synthesis. $CeO_2$ and homogeneously mixed $CeO_2$-based composites with specific surface areas of 101–152 $m^2/g$ were obtained by this synthesis method. The composites showed high oxygen storage capacities derived from high $Ce^{3+}$ contents. For their applications, the composites are used as catalyst supports for nanometal Ru and Pd for $CO_2$ methanation and $CH_4$ oxidation, respectively. Ru/$SiO_2$–$CeO_2$ demonstrated a slightly higher activity for $CO_2$ methanation, while Pd/$SiO_2$–$CeO_2$ and Pd/$Al_2O_3$–$CeO_2$ demonstrated superior low-temperature activities for $CH_4$ oxidation.

**Table of Contents**

# Chapter 1

## General Introduction

### 1–1. Metal oxides nanomaterials

In recent years, the development of functional nanosized materials with specific morphologies, high specific surface areas, and thermal stabilities has become great importance for many advanced applications. Functional nanosized materials have shown their applicability for many advanced applications due to their significantly distinct chemical, physical, electrical, and magnetic properties different from their comparable bulk materials [1]. Additionally, the large specific surface area of nanoparticles makes them advantageous for the adsorption of products and reactants [2]. Among functional nanosized materials, metal oxides have attractive features, including excellent semiconductor performance, thermal stability, and much oxygen vacancies [3]. Besides that, metal oxides have exceptional and adjustable optoelectronic, optical, electrical, thermal, magnetic, catalytic, mechanical, and photochemical properties. Hence, metal oxides have become promising materials in wide areas of chemistry, materials science, physics, and biotechnology. Numerous attempts have been made to expand the use of metal oxides across many fields due to their adaptability to obtain porous metal oxides. Various methods have been developed to alter the characteristics and control the properties of the obtained porous metal oxides and their composites. The functionality of porous metal oxides and their composites depends on their reaction conditions, metal oxide compositions, crystal structures, and morphologies [4].

## 1–2. Embedded metal nanoparticles in porous metal oxides nanomaterials

The performance of metal oxides can be tuned by porosity in metal oxides nanomaterials for practical applications. The versatility of porous metal oxides, such as large surface area, rapid mass transfer, and high storage volume, has significantly advanced science and technology and played an important role in modern society [5]. Porous metal oxides with ordered morphologies such as spheres, cubes, rods, tubes, sheets, and films are believed to offer advantageous features in terms of performance in numerous applications [6].

One application of porous metal oxides, which has been employed as supports for metal catalysts, has been expanded. Porous metal oxide nanomaterials interact not only on the exterior surface of the materials but also within the interior surface of the materials. Furthermore, a large porous volume can act as an anchor for metal catalysts to prevent the aggregation and sintering of the catalyst metals on the support surface even under harsh conditions. Embedding or encapsulating of metal catalysts into porous metal oxides is an effective approach to improve catalyst stability through physical separation of the catalyst metals [7]. Well dispersed metal nanoparticles can provide abundant active sites, which can significantly improve catalytic performance. However, in longer catalytic reactions, metal catalysts tend to be sintered, ablated, and are often accompanied by the loss of catalyst activity.

In the applications of metal oxides as catalysts and catalyst supports, single metal oxides suffer from poor stability under harsh conditions, such as high temperature environments. To overcome these issues, it was good method to combine several metal oxides. By combining several metal oxides in nanoscale as composites, an opportunity to

solve the issues and enhance the properties can be offered. Certain properties, such as lattice parameters, redox properties, thermal stabilities, surface defects, can be enhanced by mixing several metal oxides into one composite for wider applications. To control the properties of the composites, the properties, such as crystal structures and the chemical compositions of each material must be considered. Furthermore, the synthetic method also plays a role in composites' properties. Thus, the effectiveness and reproducibility of the synthesis method of metal oxides and their composites with controllable properties have been extensively studied [8].

### 1–3. Synthetic approach to embed metal nanoparticles into mixed metal oxides nanomaterials

Some synthetic methods have been developed to produce metal oxides using bottom-up chemical methods. These methods including precipitation, sol-gel, electrodeposition, solvothermal, and hydrothermal method have been examined to enhance the properties of metal oxides by controlling their particle size, pore size, surface area, dispersibility, structures, and morphology. In particular, the hydrothermal or solvothermal method would be the most effective method to synthesize nanomaterials with controllable morphology, particle size, crystal size, and structures.

Hydrothermal or solvothermal synthesis refers to the synthesis process that uses water (hydrothermal) or organic solvents (solvothermal) under high temperature conditions. Recently, countless studies using water (hydrothermal) and short-chain

alcohol-based reaction media have been extensively used to obtain functional nano-sized metal oxide particles.

However, in some cases, hydrothermal reactions tend to proceed very rapidly, which leads to difficulties in terms of controlling product properties such as crystal size, crystallinity, and aggregation [13]. Conversely, product properties are easier to control by the solvothermal method by selecting appropriate solvents. Some materials can also be employed during the solvothermal process as capping agents or additives to control the crystal growth and morphology of the nanoparticles. As a result, solvothermal synthesis using organic solvents under high-temperature conditions has become a popular synthetic method to obtain inorganic materials [14]. Adopting the versatility of the solvothermal synthetic method, a unique solvothermal synthetic methods to obtain various metal oxides as well as their composites has developed.

### 1–4. One-pot single-step solvothermal approach to embed metal nanoparticles into mixed metal oxides nanomaterials

The simple synthetic methods for submicron-sized monodisperse porous metal oxides such as $SiO_2$, $TiO_2$, $ZrO_2$, and $CeO_2$ by a one-pot and single-step solvothermal approach using organic solvents mostly ethanol and methanol has. By this synthetic approach, the following materials called **m**icro-/**m**eso-porously **a**rchitected **r**oundly **i**ntegrated **m**etal **o**xides (MARIMOs) were successfully obtained [15]. For example, $TiO_2$ MARIMO consists of ca. 5 nm primary particles with large specific surface area exceeding 300 $m^2/g$ concomitant with an almost perfect spherical morphology [16]. $TiO_2$

MARIMOs were used as a support for the Au NPs catalyst. The Au NPs catalyst prepared by the deposition-precipitation method ($Au/TiO_2$) demonstrated excellent heat tolerance and durability for highly exothermic CO oxidation, where the nano-concave-convex surface of $TiO_2$ MARIMO prevented well-dispersed Au NPs from migrating and sintering. As a result, the $Au/TiO_2$ MARIMO catalyst exhibited low-temperature activity and long-term stability as compared with Au NP catalysts supported on commercially available $TiO_2$ [17]. Besides that, perfectly monodisperse $ZrO_2$ porous spheres with large specific surface areas (244 $m^2/g$) were also successfully obtained using a similar one-pot and single-step solvothermal approach [18]. In the same manner, metal oxide assemblies were easily prepared by one-pot and single-step solvothermal reactions. When a Ru catalyst was applied to a $SiO_2$-$CeO_2$ support composite ($Ru/SiO_2$-$CeO_2$) prepared by impregnation, it exhibited low-temperature activity as well as long-term stability for $CO_2$ methanation [19].

As mentioned previously, porous metal oxides and their composites have been applied as catalyst supports for nanometal catalysts. Due to their excellent catalytic performance, well-dispersed metal catalysts in porous metal oxide supports and their composites are widely used in numerous applications such as oxidation, electrochemistry, methanation, hydrogenation, etc. However, prolonged use and harsh conditions caused sintering of the metal catalysts. Sintering of the metal catalysts start with the migration of the metal nanoparticles and their aggregation yielding larger particles. In the next stage, metal nanoparticles lose their surface area, which is a common phenomenon of the catalyst deactivation. As a result, many researchers have worked for decades to develop the method stabilizing metal catalysts.

Anti-sintering strategies to stabilize metal catalysts using chemical and physical approaches have been reported. In the chemical approaches, modification of chemical and electronic environments and structures of the catalysts and catalyst supports is a common strategy to suppress the sintering phenomena. Some anti-sintering chemical approaches, such as functionalization of organic supports, dealloying, and increase of metal-support interaction, have been reported [20]. Navarro *et al.* synthesized a cobaloxime hydrogen production catalyst through the coordination of a cobalt complex on an ethylene-bridged periodic mesoporous organosilica. The catalyst showed efficient activity for the hydrogen evolution reaction [21]. Pinedo *et al.* developed PtPd bimetallic catalysts supported on hierarchical porous carbon (HPC) with different porous sizes for the oxygen reduction reaction (ORR) toward fuel cell applications. Alloyed Pt and Pd catalysts supported on porous carbon revealed good dispersion and performance for the ORR and fuel cell applications [22]. Chen *et al.* reported that modification of the oxidizing/reducing

environment enhanced metal-support interaction between Pd and $CeO_2$ support. As a result, the catalyst demonstrated high methane oxidation abilities [23].

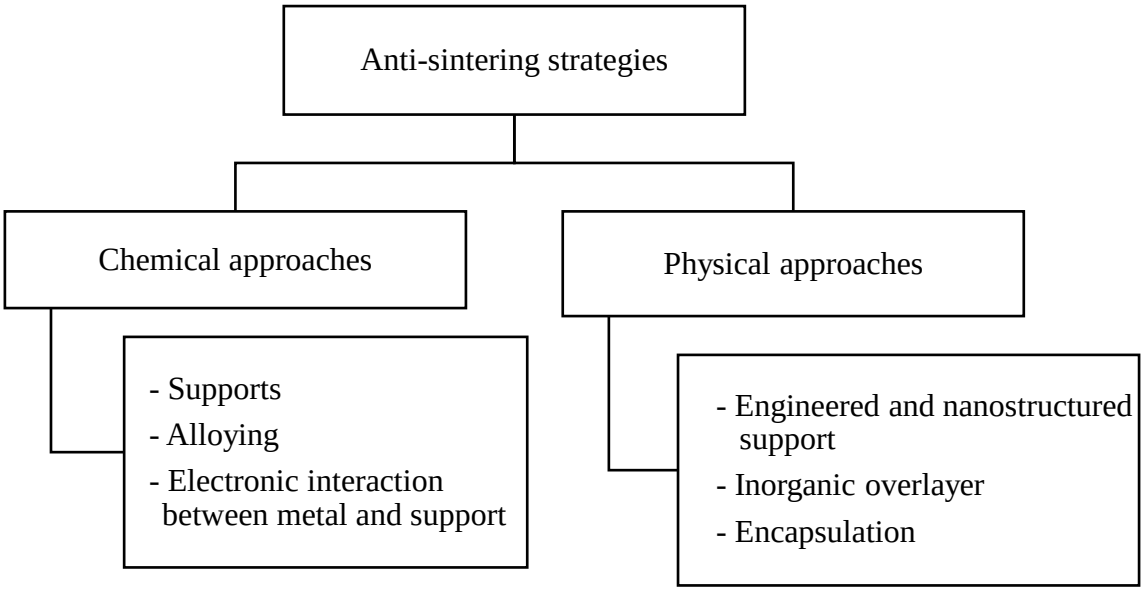


**Fig. 1-1.** Anti-sintering strategies by chemical and physical approaches

On the other hand, anti-sintering strategies using physical approaches have been developed by introducing physical barriers to modify the geometry arrangement that would increase barriers toward nanoparticle migration. The concept of an anti-sintering strategy using physical approaches can be achieved by engineered nanostructure support to maximize the migration distance by covering the catalyst active sites with inorganic layers, or by encapsulating the metal catalysts. Liu *et al.* reported a Pt NP catalyst embedded in wide-mouthed compartments tailored on a $SiO_2$ support by a reduction method as a sintering resistance NP system. Aireddi *et al.* reported that atomic layer deposition (ALD) over amorphous alumina was able to improve the alkene product selectivity of a supported Pd catalyst in acetylene ($C_2H_2$) hydrogenation [24]. Peng *et al.* fabricated a unique catalyst with Ni NPs encapsulated on a dendric mesoporous $SiO_2$ [25].

Liu *et al.* encapsulate Au NPs in a permeable $TiO_2$ thin layer by fixation on defects principle, to improve catalytic activity and stability for catalytic CO oxidation [26].

Adopting the encapsulation concept as one of the anti-sintering strategies, embedded metal catalysts in porous metal oxides and their composites in a special morphology will not only stabilize the metal catalyst and avoid the sintering process but also enhance the catalytic performances. Our one-pot and single-step solvothermal methods have attractive features, including a short reaction processing time, controllable morphology, crystallinity, and dispersibility, which can be is applicable to develop new advanced materials.

In the second chapter, a one-pot and single-step solvothermal approach using alcohol as a solvent termed "alcothermal" approach was developed to embed metal nanoparticles into $ZrO_2$ porous metal oxides and their composites. Embedded metal nanoparticles into porous metal oxides and their composites would suppress the movement of the metal nanoparticles and avoid the aggregation or sintering of metal catalyst on the support surface even under harsh conditions. Moreover, catalyst stability would improve and enhance catalytic performance. Low-temperature dry reforming of methane was selected as a probe reaction test.

In the third chapter, similar concept has been applied to embed noble metal nanoparticles into $CeO_2$ porous metal oxides and their composites using the nitrilethermal method. The term "nitrilethermal" method addresses the utilization of an aprotic polar solvent, acetonitrile, in the one-pot and single-step solvothermal methods. In this solvothermal method, acetonitrile plays a key role to control the morphology, particle size,

crystallinity, and properties of the obtained products for their application as catalysts and catalyst supports. To verify the effect of the catalyst support on the catalytic activity, two different catalytic reactions, $CO_2$ methanation and methane oxidation, were conducted.

## References


[1] N. Baig, I. Kammakakam, W. Falath, Nanomaterials: a review of synthesis methods, properties, recent progress, and challenges, Mater. Adv., 2 (2021), 1821–1871, https://doi.org/10.1039/D0MA00807A .

[2] Y. Khan, H. Sadia, S.Z. Ali Shah, M.N. Khan, A.A. Shah, N. Ullah, M.F. Ullah, H. Bibi, O.T. Bafakeeh, N.B. Khedher, S.M. Eldin, B.M. Fadhl, M.I. Khan, Classification, synthetic, and characterization approaches to nanoparticles, and their applications in various fields of nanotechnology: a review, Catalysts, 12 (2022) 1386, https://doi.org/10.3390/catal12111386.

[3] M. Rizwan, A. Shoukat, A. Ayub, B. Razzaq, M. B. Tahir, Types and classification of nanomaterials, Elsevier, 3 (2021), https://doi.org/10.1016/B978-0-12-823823-3.00001-X.

[4] S. Yin, T. Hasegawa, Morphology Control of Transition Metal Oxides by Liquid-Phase Process and Their Material Development, KONA Powder Part. J., 40 (2022) 94–108, https://doi.org/10.14356/kona.2023015.

[5] X. Weiming, Y. Shize Yang, Z. Pengfei Zhang, L. Peipei Li, W. Peiwen Wu, L. Meijun, C. Nanqing, J. Kecheng, H. Caili, Z. Ning, D. Sheng, Facile synthesis of highly porous metal oxides by mechanochemical nanocasting, Chem.Mater., 30 (2018**)** 2924–2929, https://doi.org/110.1021/acs.chemmater.7b05405.

[6] Y. Wang, H. Arandiyan, J. Scott, A. Bagheri, H. Dai, R. Amal, Recent advances in ordered meso/macroporous metal oxides for heterogeneous catalysis: a Review, J. Mater. Chem. A., 5 (2017) 8825–8846, https://doi.org/10.1039/C6TA10896B

[7] T.W Van Deelen, C.H Mejia, K.P. De Jong, Control of metal-support interactions in heterogeneous catalysts to enhance activity and selectivity, Nat. Catal., 2 (2019) 955–970, https://doi.org/10.1038/s41929-019-0364-x.

[8] S. Iravani, Surfactant-free synthesis of metal and metal oxide nanomaterials: a Perspective, RSC Sustain, 1 (2023) 72–82, https://doi.org/10.1039/D2SU00088A.

[9] J.C. Vedrine, Heterogeneous catalysis on metal oxides, Catalysts, (2017) 341–366, https://doi.org/10.3390/catal7110341.

[10] W. Su, H. Zhang, Y. Xing, X. Li, J. Wang, C. Cai, A bibliometric analysis and review of supercritical fluids for the synthesis of nanomaterials, Nanomaterials, 11 (2021), https://doi.org/10.3390/nano11020336.

[11] Y. Xu, V. Musumeci, C. Aymonier, Chemistry in supercritical fluids for synthesis of metal nanomaterials, React. Chem. Eng., 4 (2019) 2030–2054. https://doi.org/10.1039/C9RE00290A.

[12] S. Armenta, F.A.E. Turrillas, S. Garrigues, M. de la Guardia, Alternative green solvents in sample preparation, Green Anal. Chem., 1 (2022), https://doi.org/10.1016/j.greeac.2022.100007.

[13] C. Aymonier, A.L. Serani, H. Reveron, Y. Garrabos, F. Cansell, Review of supercritical fluids in inorganic materials science, J. Supercrit. Fluids, 38 (2006) 242–251, https://doi.org/10.1016/j.supflu.2006.03.019.

[14] M. Niederberger, Nonaqueous sol–gel routes to metal oxide nanoparticles, Acc. Chem. Res., 40 (2007) 793–800, https://doi.org/10.1021/ar600035e.

[15] C. Aymonier, G. Philippot, A. Erriguible, S. Marre, Playing with chemistry in supercritical solvents and the associated technologies for advanced materials by

design, J. Supercrit. Fluids, 134 (2018), 184–196, https://doi.org/10.1016/j.supflu.2017.12.021.

[16] P. Wang, K. Kobiro, Synthetic versatility of nanoparticles: a new, rapid, one-pot, single-step synthetic approach to spherical mesoporous (metal) oxide nanoparticles using supercritical alcohols, Pure Appl. Chem., 86:5 (2014) 785-800, https://doi.org/10.1515/pac-2013–1117.

[17] P. Wang, K. Kobiro, Ultimately simple one-pot synthesis of spherical mesoporous $TiO_2$ nanoparticles in supercritical methanol, Chem. Lett., 41 (2012) 264–266, https://doi.org/10.1246/cl.2012.264.

[18] F. Duriyasat, A. Irizawa, K. Hayashi, M. Ohtani, K. Kobiro, Sintering-resistant metal catalyst supported on concave-convex surface of $TiO_2$ nanoparticle assemblies, ChemCatChem, 10 (2018) 3392–3396, https://doi.org/10.1002/cctc.201800624.

[19] K. Kan, E. Yamamoto, M. Ohtani, K. Kobiro, Solvothermal synthesis of monodisperse porous zirconia spheres with large surface area, Eur. J. Inorg. Chem., 47 (2020) 4431–4435, https://doi.org/10.1002/ejic.202000813.

[20] H. Nguyen, Y. Kumabe, S. Ueda, K. Kan, M. Ohtani, K. Kobiro, Highly durable Ru catalyst supported on $CeO_2$ nanocomposites for $CO_2$ methanation. Appl Catal., 577 (2019) 33–43, https://doi.org/10.1016/j.apcata.2019.03.011.

[21] M.A. Navarro, D. Cosano, A. Bhunia, L. Simonelli, V. Martin-Diaaconescu, F.J Romero-Salguero, D. Esquivel, Cobaloxime tethered pyridine-functionalized ethylene-bridged periodic mesoporous organosilica as an efficient HER catalyst, Sustainable Energy Fuels 6 (2022) 398–407, https://doi.org/10.1039/D1SE01437D.

[22] O.M Aries-Pinedo, A.A.C Riojas, E. Pastor, E.O Lopez, G. Perez, B.S Archanjo, M. Ponce-Vargas, G.A Planes, A.M Baena-Moncada, Hierarchical porous carbon-PtPd catalysts and their activity toward oxygen reduction reaction, ACS Omega 7, (2022) 20860–20871, https://doi.org/10.1021/acsomega.2c01457.

[23] S. Chen, S. Li, R. You, Z. Guo, F. Wang, G. Li, W. Yuan, B. Zhu, Y. Gao, Z. Zhang, H. Yang, Y. Wang, Elucidation of active sites for $CH_4$ catalytic oxidation over Pd/$CeO_2$ via tailoring metal–support interactions, ACS Catal., 11 (2021) 5666–5677, https://doi.org/10.1021/acscatal.1c00839.

[24] D.R Aireddy, H. Yu, D.A Cullen, K. Ding, Elucidating the roles of amorphous alumina overcoat in palladium-catalyzed selective hydrogenation, ACS Appl Matter Interfaces, 1 (2022) 24290–24298, https://doi.org/ 0.1021/acsami.2c02132.

[25] S. Liu, W. Xu, Y. Niu, B. Zhang, L. Zheng, W. Liu, L. Li, J. Wang, Ultra stable Au nanoparticles on titania through an encapsulation strategy under oxidative atmosphere, Nat Commun., 10 (2019) 5790–5799, https://doi.org/10.1038/s41467-019-13755-5.

[26] H. Peng, X. Zhang, X. Han, X. You, S. Lin, H. Chen, W. Liu, X. Wang, N. Zhang, Z. Wang, P. Wu, H. Zhu, S. Dai, Catalysts in coronas: a surface spatial confinement strategy for high-performance catalysts in methane dry reforming, ACS Catal., 9 (2019) 9072–9080, https://doi.org/10.1021/acscatal.9b00968.

# Chapter 2

## One-Pot Single-Step Alcothermal Synthesis to Embed Ni Catalysts in $ZrO_2$ Porous Spheres and Their Activity in Low-temperature Dry Reforming of Methane

### 2–1. Introduction

The combination of metal nanoparticles (NPs) and metal oxides as catalyst supports to produce heterogeneous catalysts exhibits excellent catalytic activity in many practical uses [1]. However, the attachment of metal NPs on the surface of the catalyst supports tends to aggregate and sinter under harsh conditions, such as high temperatures and long reaction time. Embedding or encapsulating NPs in porous metal oxides could be an option to avoid this aggregation and sintering phenomenon by improving catalyst stability and preventing physical separation of the metal NPs from the catalyst support [4]. Basically, the idea to embed or encapsulate NPs entails physically wrapping the metal NPs in three-dimensional cages to suppress the migration leading to sintering. Hence, embeding metal NPs in the pores of base metal oxides, could be one of the effective approaches to improve catalyst stability and avoid catalyst sintering. As a result, several studies have been devoted to develop strategies to encapsulate metal NPs into metal oxide supports. For example, Liu *et al.* encapsulated Au NPs in the permeable $TiO_2$ thin layer to yield highly active and stable catalysts for catalytic CO oxidation (Fig. 2-1a) [5]. Liu *et al.* reported a Pt NP catalyst embedded in wide-deep well $SiO_2$ support as a sintering resistance NP system (Fig. 2-1b) [6]. Yin *et al.* prepared an embedded Pt supported on carbon (Fig. 2-1c) and discovered that enlarging the particle distance beyond the critical distance suppressed the particle coalescence [7].

Once catalyst stability improved and physical separation of the metal can be avoided, heterogeneous catalysts with high performance and stability can be used in various catalytic processes, even under harsh conditions and prolonged reaction times, for instance, the dry reforming of methane (DRM, Eq. 1). DRM is a highly endothermic reaction that converts two greenhouse gases ($CH_4$ and $CO_2$) into CO and $H_2$ [8].

$$CH_4 + CO_2 \rightarrow 2CO + 2H_2 \quad (1)$$

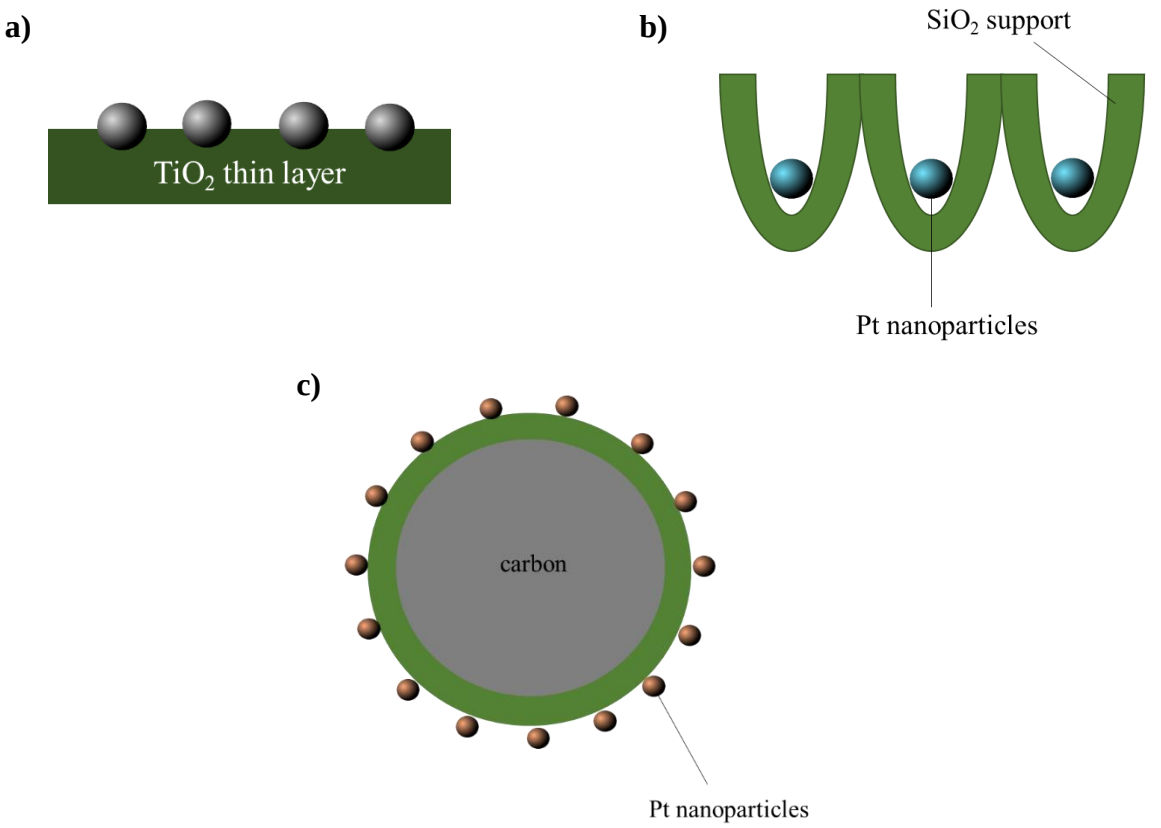


**Fig. 2-1. a)** Pt NP catalyst embedded in $TiO_2$ thin layer support, **b)** Pt NP catalyst embedded in wide-deep well $SiO_2$ support, and **c)** Pt NP catalyst supported on carbon.

Ni catalysts supported on several oxides are commonly used in the DRM since they are highly active and less expensive than noble metal catalysts. However, the carbon deposition became a serious drawback in practical applications. High temperature

conditions of around 700°C is favorable to avoid the formation of carbon species. On the other hand, Ni nanometal is prone to sinter at this temperature. Therefore, it is necessary to improve Ni-based catalyst stability in order to obtain a highly active Ni-based catalysts with good carbon suppression ability and sintering resistance.

Few attempts have been performed to resolve these problems. Liu *et al*. prepared a core-shell catalyst with Ni-$ZrO_2$@microporous $SiO_2$ structure [9]. Peng *et al.* fabricated a unique catalyst with Ni NPs confined on a dendric mesoporous $SiO_2$ [10]. Lin *et al.* also developed a core-shell catalyst with Ni-$CeO_2$@microporous $SiO_2$ structure [11]. Liu *et al*. reported an intermetallic alloy nanocatalyst ($In_xNi$@$SiO_2$) [12]. From these studies, lead to the conclusion that the exposed Ni NPs on the flat surface of the support may react with the excess methane molecules during the reaction, resulting in the accumulation of carbon atoms as nickel carbide to lead carbon deposition and catalyst deactivation. This issue can be avoided by encapsulation Ni NPs in a spatial support.

In this study, a one-pot and one-step solvothermal synthesis method using alcohols as solvents termed "alcothermal" has been developed to embed Ni NPs into composite metal oxide supports. By embedding Ni NPs into composite metal oxide supports, the formation of carbon species could be physically prevented as illustrated in Fig. 2-2. The obtained catalysts were investigated for dry reforming of methane at low temperatures.

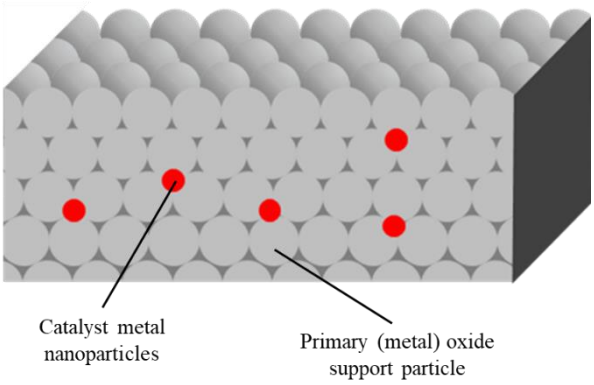

**Fig. 2-2.** Schematic of embedded nanometal in the gaps of primary (metal) oxide support nanoparticles.

$ZrO_2$ porous spheres were chosen as catalyst supports. Additional elements were combined with $ZrO_2$ to create composites in expectation of higher heat tolerance than $ZrO_2$ itself to achieve better catalytic activity and stability. For instance, MgO–$ZrO_2$ composite was chosen as a catalyst support in anticipation of positive acid-base interactions between $CO_2$ and MgO [13,14], $SiO_2$–$ZrO_2$ composite was chosen as a catalyst support to increase the surface area, and $Y_2O_3$–$ZrO_2$ served as a long-life catalyst support by inhibiting the sintering of the catalyst support, respectively.

## 2–2. Experiment

### 2–2–1. Materials

85% zirconium butoxide 1-butanol solution, nickel (II) nitrate hexahydrate, and tetraethoxysilane were purchased from Fujifilm Wako Chemical Corporation. Yttrium isopropoxide, acetylacetone, and magnesium acetylacetonate were purchased from Tokyo Chemical Industry Corporation. Ethanol was purchased from Kishida Chemical Corporation. UEP-100 $ZrO_2$ NPs were obtained from Daiichi Kigenso Kagaku Kogyo Co., Ltd. All reagents were used without further purification.

### 2–2–2. Catalyst Preparation

A precursor solution including 85 wt% zirconium butoxide in 1-butanol (3.20 g, 7.09 mmol), acetylacetone (50 mL, 0.48 mmol), and $Ni(NO_3)_2 \cdot 6H_2O$ (500 mg, 1.68 mmol) in ethanol (35 mL) was heated in an SUS-316 stainless steel autoclave (MMS-5000, OM LAB-TECH Co., Ltd.) at 250 °C for 60 min, where the quantity of Ni salt was adjusted to Ni/support metal oxide(s) = 10/90 (*wt*/*wt*). The reactor was then cooled to

room temperature. The obtained solid was centrifuged at 10,000 rpm for 15 min at 25 °C and washed three times with methanol. The solid was dried under vacuum for 20 h at room temperature to yield a powdery product, which is denoted as Ni@$ZrO_2$. Then Ni@$ZrO_2$ was calcined at 300 °C for 2 h in air. Ni catalysts supported on $SiO_2$–$ZrO_2$, MgO–$ZrO_2$, and $Y_2O_3$–$ZrO_2$ composite porous spheres were prepared as follows: tetraethoxysilane (156 μL, 0.703 mmol), magnesium acetylacetonate (155 μL, 0.699 mmol), or yttrium isopropoxide (18.6 mg, 0.700 mmol) was dissolved in ethanol (85 mL). 85 wt% zirconium butoxide solution in 1-butanol (2.84 g, 6.29 mmol), acetylacetone (50 mL, 0.48 mmol), and an ethanol (35 mL) solution of $Ni(NO_3)_2 \cdot 6H_2O$ (445 mg, 1.53 mmol) were added to the solution successively to produce a precursor solution, in which the Si, Mg, or Y content was adjusted to (Si, Mg, or Y)/Zr = 1/9 (mol/mol). Similar solvothermal treatment of the precursor solutions afforded the Ni catalysts supported on the porous composite spheres, Ni@$SiO_2$–$ZrO_2$-C, Ni@MgO–ZrO-C, and Ni@$Y_2O_3$–$ZrO_2$-C, where "@" and "C" represents "prepared by solvothermal method" and "composites" respectively.

Ni catalysts supported on small porous spheres were obtained according to a similar procedure to that mentioned above except for the addition of water (3 mL) to the precursor solutions. The prepared small catalysts are referred to as Mini Ni@$ZrO_2$, Mini Ni@$SiO_2$−$ZrO_2$-C, Mini Ni@MgO−$ZrO_2$-C, and Mini Ni@$Y_2O_3$−$ZrO_2$-C. Reference Ni catalysts supported on UEP-100 $ZrO_2$ and $ZrO_2$ porous spheres were prepared by the impregnation method. A mixture of 131 mg (0.451 mmol) $Ni(NO_3)_2 \cdot 6H_2O$ and 500 mg UEP-100 $ZrO_2$ or $ZrO_2$ porous spheres in 12.5 mL of water was mixed well using a planetary centrifugal mixer (Thinky AR-100) for 2 h. The obtained powder was dried in air at 80 °C for 2 h and then calcined in air at 300 °C for 2 h to produce a Ni catalyst, U-

$Ni/ZrO_2$ or $Ni/ZrO_2$, where "/" represents "obtained by impregnation method."

### 2–2–3. Catalyst characterization

Transmission electron microscopy (TEM) images were obtained using a JEOL JEM-2100F microscope. Energy-dispersive X-ray (EDX) spectroscopy was performed using an Oxford INCA X-Max 80 EDX spectrometer with the TEM instrument. Scanning electron microscopy (SEM) images were obtained using a Hitachi SU8020 FE-SEM. Inductively coupled plasma optical emission spectroscopy (ICP-OES) was performed using a Hitachi High-Tech Science PS3520UV-DD spectrometer. Elemental analysis was carried out on a Malvern Panalytical Epsilon 1 X-ray fluorescence (XRF) spectrometer. Nitrogen adsorption/desorption experiments were conducted using a BEL BELSORP mini II instrument. The specific surface area was calculated by the Brunauer–Emmett–Teller method using the obtained nitrogen adsorption-desorption isotherms. The crystalline phases of the catalysts were identified by X-ray diffraction (XRD) on a Rigaku SmartLab diffractometer using Cu-Kα radiation. The data were recorded over a $2\theta$ range of 10° to 90°.

### 2–2–4. Catalytic reaction

Catalytic activity tests for DRM were performed using a flow-type reactor, MicrotracBEL BELCAT II. Prior to reaction, the catalyst (100 mg) was loaded in a tubular reactor (inner diameter = 7.5 mm) and fixed with quartz wool on both sides. Then, the catalyst was reduced by $H_2$ at 30 mL/min flow at 450 °C for 2 h. The DRM was conducted at 550 °C under a mixed gas stream of $CO_2/CH_4/N_2$=10/10/5 (*v*/*v*/*v*) with a

total gas flow rate of 25 mL/min. The temperature of the reactor was maintained at 550 °C for 15 h. The gaseous products were analyzed using a gas chromatograph (GL Sciences GC3200) with an active carbon column equipped with a TCD.

The $CH_4$ and $CO_2$ reaction frequencies were estimated by the moles of $CH_4$ or $CO_2$ converted per second per the moles of catalysts with the following equation:

$$\text{Reaction frequencies} = \frac{N\,(\text{gas})}{N\,(\text{catalyst})} \times \text{conversion}$$

where $N$ (gas), $N$ (catalyst), and conversion represent gas flow (mol/s) the amount of catalyst (mol), and the conversion of reactant gas, respectively.

## 2–3. Results and discussion

### 2–3–1 Catalyst preparation

Ni NPs embedded in $ZrO_2$ were obtained using three different synthesis methods. First, embedded Ni NPs in $ZrO_2$ was obtained by the impregnation method. The impregnation method is known as a versatile method to attach metal NPs into a catalyst support. In this study, the impregnation method was employed to attach an Ni catalyst to the surface of commercially available UEP-100 $ZrO_2$ support to yield U-Ni/$ZrO_2$. Second, a one-pot single step solvothermal method was combined with the impregnation method to attach the Ni NPs to the $ZrO_2$ porous spheres. The $ZrO_2$ porous spheres were prepared by the one-pot single step solvothermal method. Then, Ni NPs were attached to the surface of $ZrO_2$ porous sphere by impregnation to obtained Ni/$ZrO_2$ [15]. Third, a one-pot single step solvothermal method using ethanol as a solvent termed "alcothermal" was employed to embed the Ni NPs into $ZrO_2$ and its composites.

In this alcothermal method, the principle of the co-precipitation technique was adopted to prepare noble metal catalysts supported on base metal oxides [16]. More specifically, a mixed solution of a noble metal salt and a base metal salt was neutralized by an alkaline solution to yield a coprecipitate containing mixed hydroxides of both metals. The coprecipitate was calcined to produce a noble metal catalyst supported on a base metal oxide. A precursor solution containing $Ni(NO_3)_2$ and $Zr(O^nBu)_4$ in ethanol was heated at 250 °C to yield Ni@$ZrO_2$. The obtained material was washed using methanol and calcined at 300 °C for 2 h in air to remove organic residues. According to the similar manner, Ni catalysts embedded in $ZrO_2$ composites, such as Ni@$SiO_2$–$ZrO_2$-C, Ni@MgO–$ZrO_2$-C, and Ni@$Y_2O_3ZrO_2$-C, were obtained from the precursor solutions by adding additional oxides sources such as tetraethoxy silane, magnesium

**Table 1** Crystallite size, specific surface area, pore volume, secondary particle size, and element contents of Ni catalyst supported on $ZrO_2$-based porous spheres.

| Materials[1)] | Secondary Particle size[2)] (nm) | Specific surface area[3)] ($m^2/g$) | | Pore volume[4)] ($cm^3/g$) | Element content[5)] | | | | |
|---|---|---|---|---|---|---|---|---|---|
| | | Before $H_2$ reduction | After $H_2$ reduction | | Ni[5,6)] | Si[5,7)] | Mg[5,7)] | Y[5,7)] | Zr[5,7)] |
| Ni@$ZrO_2$ | 602 ± 63 | 71 | 4 | < 0.1 | 9.5 | – | – | – | 100 |
| Ni@$SiO_2$–$ZrO_2$-C | 700 ± 61 | 135 | 2 | < 0.1 | 8.4 | 5.6 | – | – | 94.4 |
| Ni@MgO–$ZrO_3$-C | 618 ± 59 | 114 | 6 | 0.18 | 8.9 | – | 11.9 | – | 88.1 |
| Ni@$Y_2O_3$–$ZrO_2$-C | 710 ± 120 | 238 | 4 | 0.88 | 6.5[8)] | – | – | 9.0[8)] | 91.0[8)] |
| Mini Ni@$ZrO_2$-C | 120 ± 50 | 179 | 140 | 0.87 | 9.0 | – | – | – | 100 |
| Mini Ni@$SiO_2$–$ZrO_2$-C | 63 ± 18[9)] | 269 | 196 | 0.47 | 9.0 | 6.1 | – | – | 93.9 |
| Mini Ni@MgO–$ZrO_2$-C | 83 ± 25 | 167 | 151 | 0.28 | 6.6 | – | 11.5 | – | 98.5 |
| Mini Ni@$Y_2O_3$–$ZrO_2$-C | 115 ± 36 | 267 | 130 | 0.35 | 6.5[8)] | – | – | 9.6[8)] | 90.4[8)] |
| U-Ni/$ZrO_2$[10)] | [11)] | 76 | 73 | 0.36 | 8.2 | – | – | – | – |
| Ni/$ZrO_2$[12)] | 1340 ± 130 | 20 | 3 | < 0.1 | 8.4 | – | – | – | – |

1) Materials were used after calcination in air at 300 °C for 1 h. 2) As prepared materials. Evaluated by SEM images of at least 100 particles. 3) Brunauer–Emmett–Teller method. 4) BJH method. 5) Fluorescent X-ray analysis. 6) Weight %. 7) Atomic ratio of Si, Mg, or Y *vs.* Zr. 8) ICP-OES method. 9) Evaluated by TEM images of at least 100 particles. 10) Ni NPs were supported on commercially available $ZrO_2$ (UEP-100) by impregnation method. 11) Not measured. 12) Ni NPs were supported by an impregnation on $ZrO_2$ porous spheres obtained by a solvothermal method.

acetylacetonate, and yttrium isopropoxide, respectively. The physical properties of the obtained materials including estimated secondary particle sizes, specific surface areas, pore volumes, and elemental content were observed and the results are provided in Table 1.

The morphology of U-Ni/$ZrO_2$, Ni/$ZrO_2$, Ni@$ZrO_2$, and $ZrO_2$-based composites were observed by SEM and TEM (Fig. 2-3). Ni@$ZrO_2$ showed an almost perfect spherical morphology with 600–700 nm diameters. U-Ni/$ZrO_2$ (Fig. 2-3e) showed a small aggregate of primary NPs. The Ni contents of the catalysts were assessed using STEM/EDX and XRF. From elemental analyses by XRF, the Ni content of U-Ni/$ZrO_2$ Ni/$ZrO_2$ was around 8.2 wt% and 8.4 wt% comparable to the precursor solutions (10.0 wt% of Ni). Meanwhile, Ni@$ZrO_2$ and its composites showed a uniform dispersion of Ni atoms throughout the spheres with 9.5 wt% content. The STEM/EDX results (Fig. 2-4) indicate that Ni, Si, Mg, and Y atoms were distributed homogeneously across the network of porous spheres. XRF or ICP-OES analysis (Table 1) revealed that the embedded Ni contents of the catalysts obtained by the solvothermal method were more than 8 wt% in the cases of Ni@$SiO_2$–$ZrO_2$-C and Ni@MgO–$ZrO_2$-C, while that of Ni@$Y_2O_3$–$ZrO_2$-C was slightly smaller (6.5 wt%). The Si content was ca. 6 wt% and the Mg and Y content were 9–12 wt%, which are similar to the corresponding content (10 wt%) in the precursor solutions.

The XRD patterns of U-Ni/$ZrO_2$ (Fig. 2-7i), Ni/$ZrO_2$ (Fig. 2-7j), Ni@$ZrO_2$ (Fig 2-7a, and its composites revealed a monoclinic and cubic $ZrO_2$, respectively. From Fig. 2-7, no peaks corresponding to cubic Ni were observed in the XRD pattern Ni/$ZrO_2$, Ni@$ZrO_2$ and its composites. According to the Scherrer's equation, Ni crystallite sizes are very small (< 5 nm), hence Ni peak was not observed on the XRD pattern.

However, $H_2$ reduction at 450 °C for 2 h sintering of the $ZrO_2$ primary particles and Ni particles occurred, resulting in the narrowing of the $ZrO_2$ peaks and Ni peak were observed in the Ni/$ZrO_2$ and Ni@$ZrO_2$ samples. However, in the cases of Mini Ni@MgO–$ZrO_2$-C, Mini Ni@$SiO_2$–$ZrO_2$-C, and Mini Ni@$Y_2O_3$–$ZrO_2$-C, the absence of the peak related to Ni species after high-temperature reduction indicate that Ni particles on those catalysts remained small even after $H_2$ reduction at 450 °C.

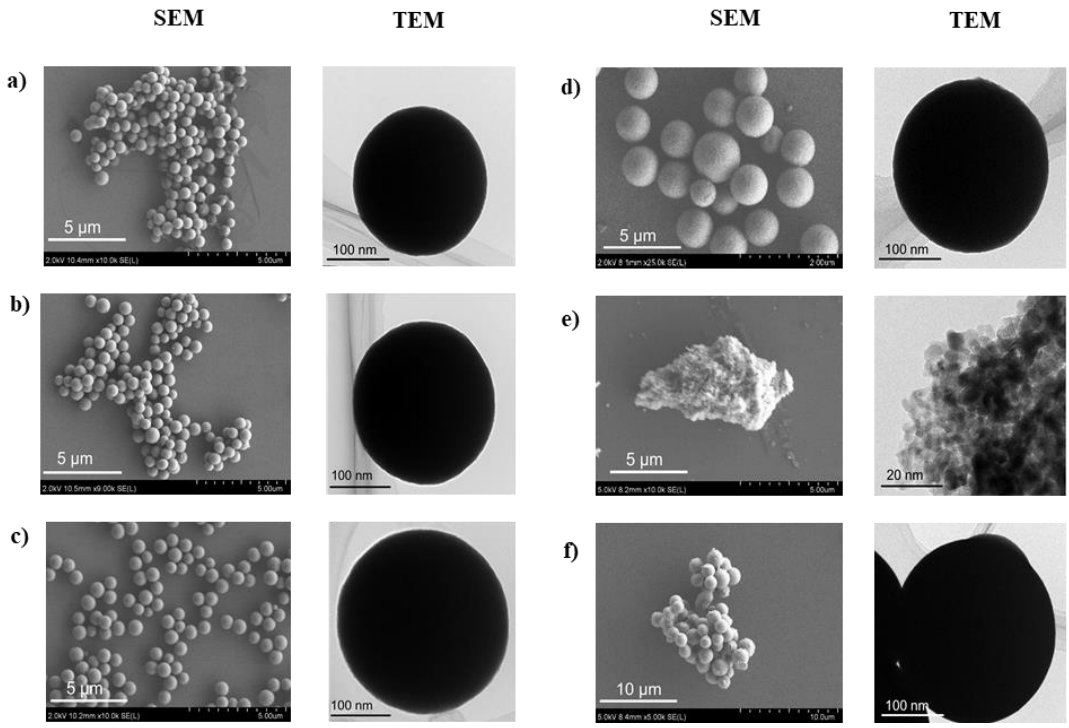


**Fig. 2-3.** SEM and TEM images of Ni catalysts embedded in Ni@$ZrO_2$-based composites. **a)** Ni@$ZrO_2$, **b)** Ni@$SiO_2$–$ZrO_2$-C, **c)** Ni@MgO–$ZrO_2$-C, **d)** Ni@$Y_2O_3$–$ZrO_2$-C, **e)** U-Ni/$ZrO_2$, and **f)** Ni/$ZrO_2$.

The specific surface areas of the catalysts were analyzed using BET method. U-Ni/$ZrO_2$ showed a specific surface area of 76 $m^2/g$ being higher than the specific surface area of Ni/$ZrO_2$ (20 $m^2/g$). Interestingly, Ni@$ZrO_2$-based composites exhibited higher

specific surface areas (71–240 $m^2/g$). However, the high specific surface areas were drastically reduced to 2–6 $m^2/g$ when the catalysts were reduced by $H_2$ at 450 °C for 2 h due to the sintering of the $ZrO_2$ NPs and Ni NPs. Conversely, the specific surface area of U-Ni/$ZrO_2$ did not change (73 $m^2/g$) even after calcination in air.

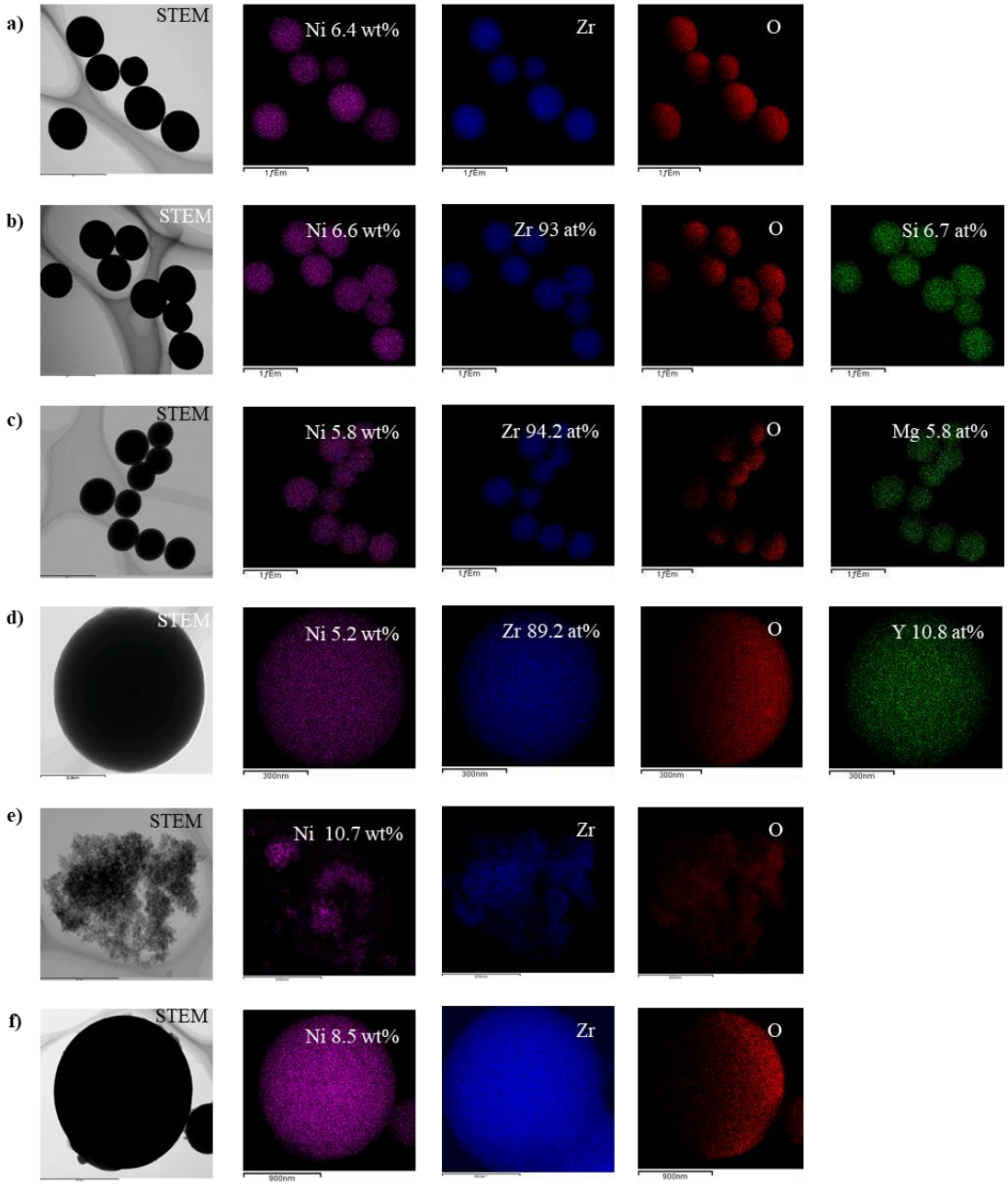


**Fig. 2-4.** STEM/EDX and TEM images of as-prepared Ni@$ZrO_2$-based composites. **a)**

Ni@$ZrO_2$, **b)** Ni@$SiO_2$–$ZrO_2$-C, **c)** Ni@MgO–$ZrO_2$-C, **d)** Ni@$Y_2O_3$–$ZrO_2$-C, **e)** U-Ni/$ZrO_2$, and **f)** Ni/$ZrO_2$.

Since the $H_2$ reduction dramatically reduced the specific surface area of the catalysts, $ZrO_2$ porous spheres with smaller primary particles would tolerate sintering even at high temperatures and this characteristic would be more effective for gas sorption of porous sphere catalysts. Therefore, $ZrO_2$ with smaller spherical secondary particles were synthesized by adding a small amount of water to the precursor solutions. The Ni catalysts embedded in the smaller porous supports are denoted as Mini Ni@$ZrO_2$-C, Mini Ni@$SiO_2$–$ZrO_2$-C, Mini Ni@MgO–$ZrO_2$-C, and Mini Ni@$Y_2O_3$–$ZrO_2$-C.

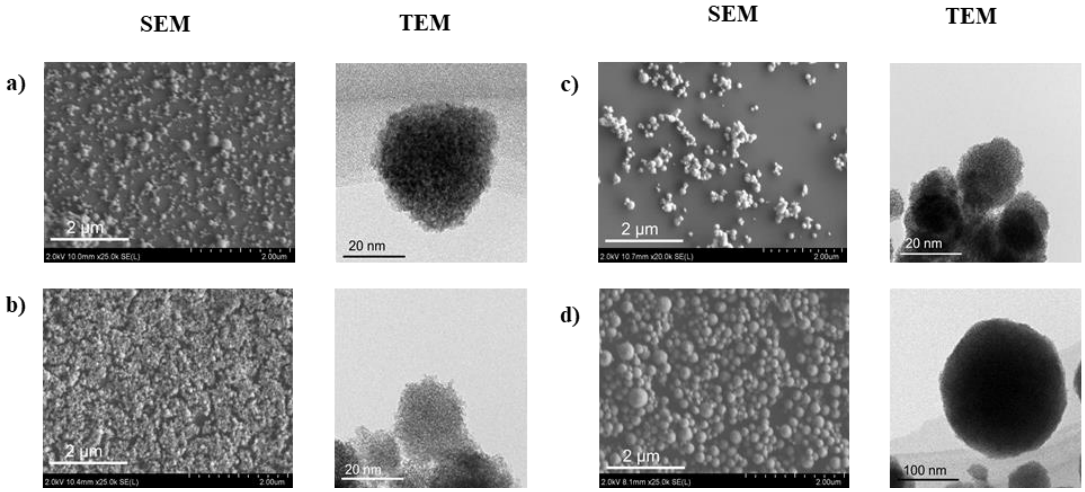


**Fig. 2-5.** SEM and TEM images of Mini-series of Ni@$ZrO_2$-based composites, **a)** Mini Ni@$ZrO_2$, **b)** Mini Ni@$SiO_2$–$ZrO_2$-C, **c)** Mini Ni@MgO–$ZrO_2$-C, and **d)** Mini Ni@$Y_2O_3$–$ZrO_2$-C.

The mechanism of the alcothermal reaction of Ni@$ZrO_2$ can be explained as follows: $Ni(NO_3)_2$ and $Zr(O^nBu)_4$ hydrolyzed by $H_2O$, which is generated through the condensation of ethanol at a high temperature, to yield hydroxides from both metals. The

nuclei particles aggregate and condense with each other, yielding monodispersed spheres with uniform particle sizes of corresponding metal oxides at the nanoscale level. Then, under solvothermal conditions nickel hydroxide and/or nickel oxide in the mixed oxides can be reduced by high-temperature ethanol, generating embedded Ni metal NPs in $ZrO_2$ porous sphere supports.

Meanwhile, the addition of the small amount of water in the alcothermal synthesis increases the hydrolysis rate and forms a new nucleus generating polydisperse spheres with smaller particle sizes of metal oxides. As a result, the secondary particle sizes decreased from 600–700 nm to 63–120 nm to yield mini composites (Fig. 2-3 and 2-5). The dispersion of Ni atom in Mini-series of Ni@$ZrO_2$ are 6.5–9.0 wt% (Fig. 2-6). XRD patterns of Mini-series of Ni@$ZrO_2$ (Mini Ni@$ZrO_2$, Mini Ni@$SiO_2$–$ZrO_2$-C, Mini Ni@MgO–$ZrO_2$-C, and Mini Ni@$Y_2O_3$–$ZrO_2$-C) are shown in Fig. 2-7. In Fig. 2-7Aa-h, Mini-series of Ni@$ZrO_2$ showed a broader peak than those of the large porous spheres (Ni@$ZrO_2$, Ni@$SiO_2$–$ZrO_2$-C, Ni@MgO–$ZrO_2$-C, and Ni@$Y_2O_3$–$ZrO_2$-C), indicating that the crystallite size of the $ZrO_2$ primary particles in the small porous sphere slightly increased.

In XRD pattern, the absence of Ni peaks was also observed for Mini Ni@$ZrO_2$ and Mini Ni@MgO–$ZrO_2$-C (Fig. 2-7Ae,g). The absence of Ni peaks was recognized in the cases of Mini Ni@$SiO_2$-$ZrO_2$-C and Mini Ni@$Y_2O_3$–$ZrO_2$-C (Fig. 2-7Af,h) as well. The XRD profiles of the Mini-series of Ni@$ZrO_2$ were very broad (Fig. 2-7Ae-h). Moreover, a cubic Ni phase was observed in the cases of Mini Ni@$ZrO_2$ and Mini Ni@MgO–$ZrO_2$-C. The absence of Ni peaks was observed in the cases of Mini Ni@$SiO_2$–$ZrO_2$-C (Fig. 2-7Bf) and Mini Ni@$Y_2O_3$–$ZrO_2$-C (Fig. 2-7Bh), even after $H_2$ reduction at

450 °C for 2 h, suggesting that the small series catalysts are high-temperature-resistant catalysts.

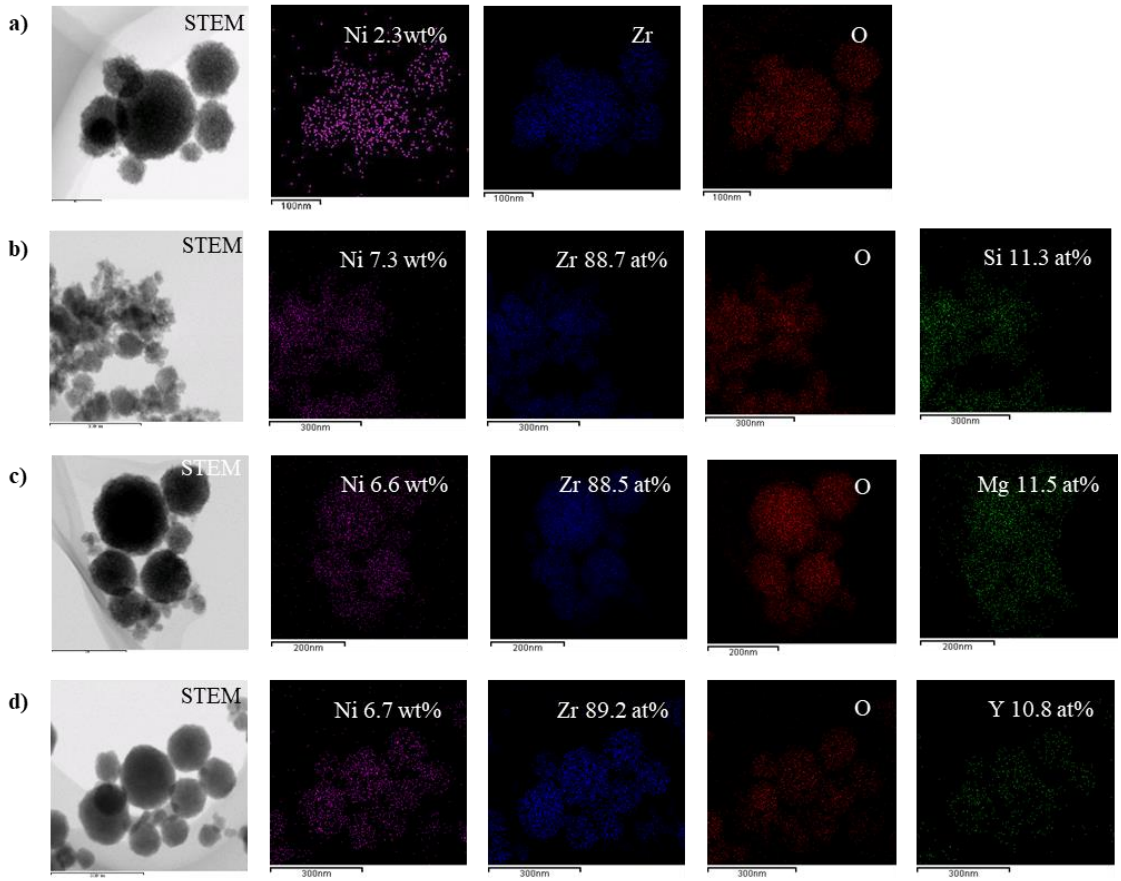


**Fig. 2-6.** STEM/EDX images of as-prepared Ni catalysts embedded in Mini-series $ZrO_2$-based composites. **a)** Mini Ni@$ZrO_2$, **b)** Mini Ni@$SiO_2$–$ZrO_2$-C, **c)** Mini Ni@MgO-$ZrO_2$-C, and **d)** Mini Ni@$Y_2O_3$–$ZrO_2$-C.

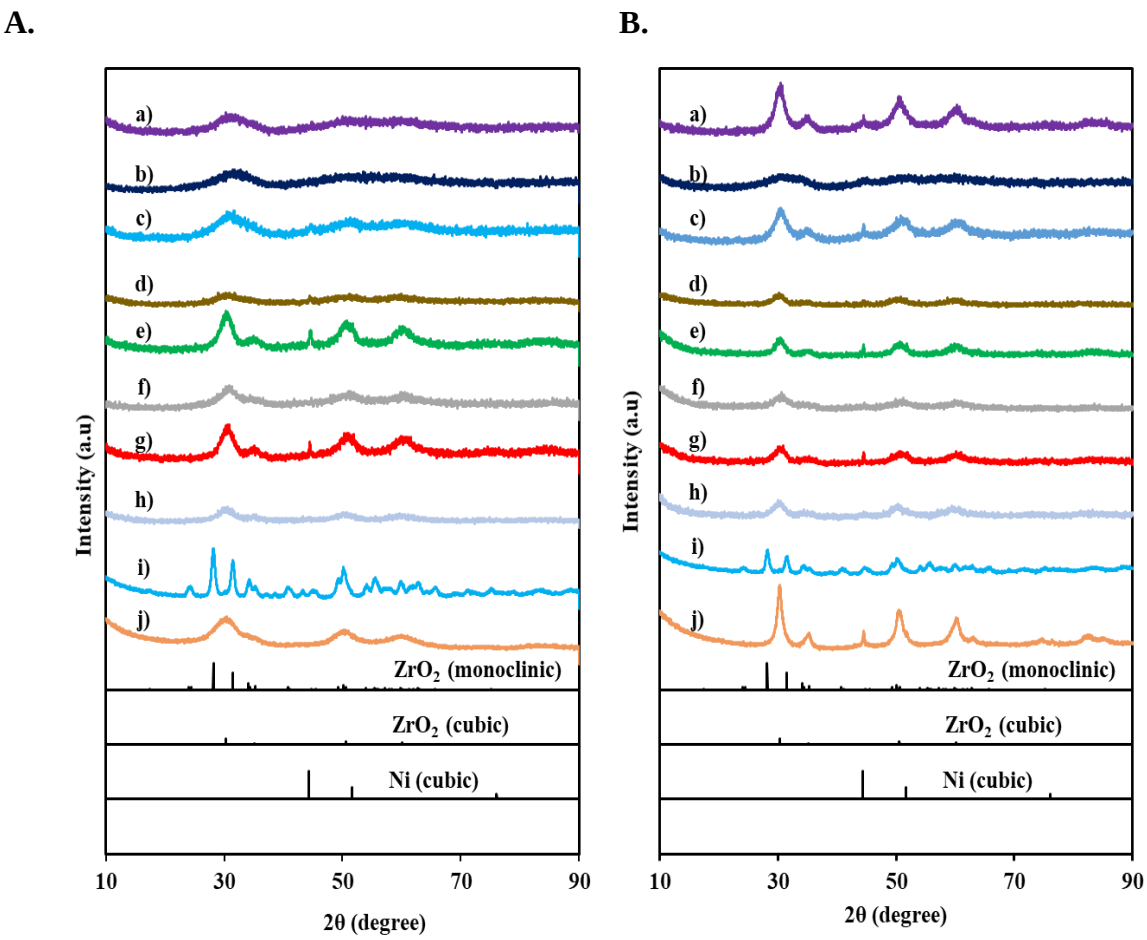


**Fig. 2-7.** XRD patterns of Ni@$ZrO_2$-based composites. **A)** Before $H_2$ reduction and **B)** after $H_2$ reduction. **a)** Ni@ $ZrO_2$, **b)** Ni@$SiO_2$–$ZrO_2$-C, **c)** Ni@MgO–$ZrO_2$-C, **d)** Ni@$Y_2O_3$–$ZrO_2$-C, **e)** Mini Ni@$ZrO_2$, **f)** Mini Ni@$SiO_2$–$ZrO_2$-C, **g)** Mini Ni@MgO–$ZrO_2$-C, **h)** Mini Ni@$Y_2O_3$–$ZrO_2$-C, **i)** U-Ni/$ZrO_2$, and **j)** Ni/$ZrO_2$.

### 2–3–2. DRM reaction

DRM reaction was employed to further understand the impact of the embedded morphology of Ni NPs in $ZrO_2$-based porous spheres. In addition, DRM reaction was

carried out at a lower temperature (550 °C) to examine the suppressive effects on carbon deposition.

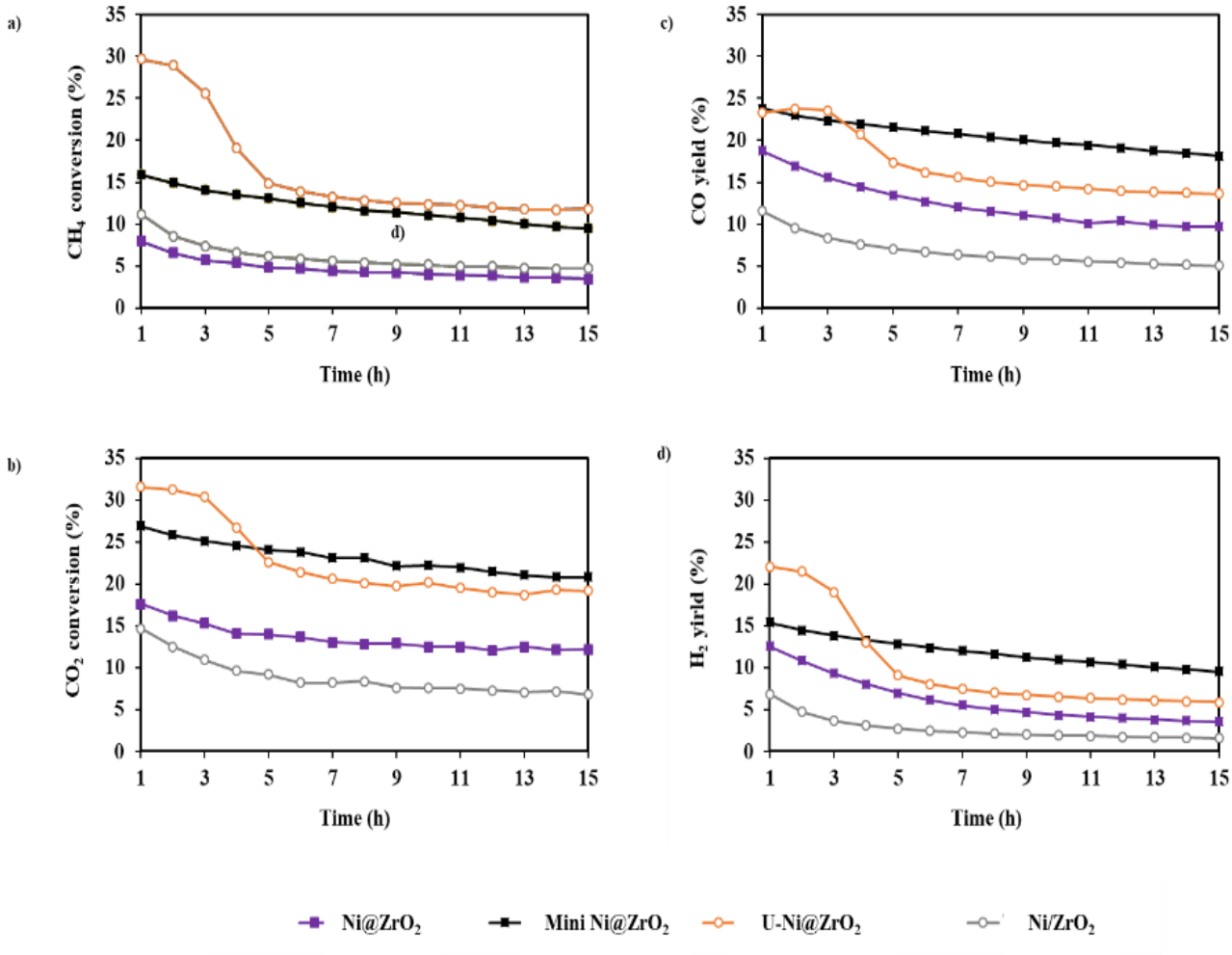


**Fig. 2-8.** DRM reactions catalyzed by Ni@$ZrO_2$, Mini Ni@$ZrO_2$, U-Ni@-$ZrO_2$, and Mini Ni@$ZrO_2$. **a)** $CH_4$ conversions, **b)** $CO_2$ conversions, **c)** CO yields, and **d)** $H_2$ yields.

The catalytic activity of U-Ni/$ZrO_2$, Ni/$ZrO_2$, Ni@$ZrO_2$, and Mini Ni@$ZrO_2$ toward DRM reaction are shown in Fig. 2-8. At the very beginning of the reaction, U-Ni/$ZrO_2$ catalyst, which is prepared by impregnation from commercially available UEP-100 $ZrO_2$ support, performed the highest catalytic ability in both $CO_2$ and $CH_4$ conversions along with the highest CO and $H_2$ yields. Nevertheless, the catalytic ability gradually decreased after a 5h reaction time. Ni/$ZrO_2$ and Ni@$ZrO_2$ prepared by

impregnation from $ZrO_2$ porous spheres (two-step preparation method) and solvothermal method, respectively, showed relatively lower catalytic abilities in $CO_2$ and $CH_4$ conversions as well as CO and $H_2$ yields.

Among those catalysts (Ni@$ZrO_2$, Mini Ni@$ZrO_2$, U-Ni@-$ZrO_2$, and Mini Ni@$ZrO_2$), Mini Ni@$ZrO_2$ performed high activity in both $CH_4$ and $CO_2$ conversions together with high CO and $H_2$ yields as compared to Ni/$ZrO_2$ and embedded Ni@$ZrO_2$ (Fig. 2-9). The substantially higher specific surface area of Mini Ni@$ZrO_2$ (140 $m^2$/g after $H_2$ reduction) than those of Ni/$ZrO_2$ (3 $m^2$/g after $H_2$ reduction and Ni@$ZrO_2$ (4 $m^2$/g after $H_2$ reduction) can be attributed to the significant difference in their catalytic activities.

On the other hand, compared to Mini Ni@$ZrO_2$, the Mini-series catalysts (Mini Ni@$SiO_2$–$ZrO_2$-C, Mini Ni@MgO–$ZrO_2$-C, and Mini Ni@$Y_2O_3$–$ZrO_2$) performed better catalytic activities. As seen in Fig. 2-9, the results can be divided into two categories; those with a lower performance, such as Mini Ni@$ZrO_2$ and Mini Ni/MgO–$ZrO_2$-C, and those with a higher performance, such as Mini Ni@$SiO_2$–$ZrO_2$-C and Mini Ni@$Y_2O_3$–$ZrO_2$-C. The reactions catalyzed by Mini Ni@$SiO_2$–$ZrO_2$-C and Mini Ni@$Y_2O_3$–$ZrO_2$-C and the yields of CO and $H_2$ were consistent for 15 hours, but the reactions catalyzed by Mini Ni@$ZrO_2$ and Mini Ni/MgO–$ZrO_2$-C gradually declined with time.

The higher catalytic activity of Mini-series catalysts can be explained by several factors such as a higher surface area exceeding 100$m^2$/g even after $H_2$ reduction compared to the other catalyst prepared by impregnation and solvothermal method. The other factors that caused the higher catalytic activity of Mini-series catalysts can be explained by the smaller primary particles and Ni metal NPs that perfectly dispersed on the surface and the

gap of primary particles as shown in Fig. 2-2, which is effective for gas sorption of porous sphere catalysts. The reaction frequencies of Ni@$ZrO_2$, Mini-series of Ni@$ZrO_2$ estimated the activity per available surface Ni atom per unit time is independent of Ni particle size for the DRM. The reaction turnover of Mini-series Ni@$ZrO_2$ as a catalyst were summarized in Table 2. The values were comparable to a representative low temperature DRM catalyzed by Ni catalyst supported on $SiO_2$–$ZrO_2$ obtained by co-impregnation method [17].

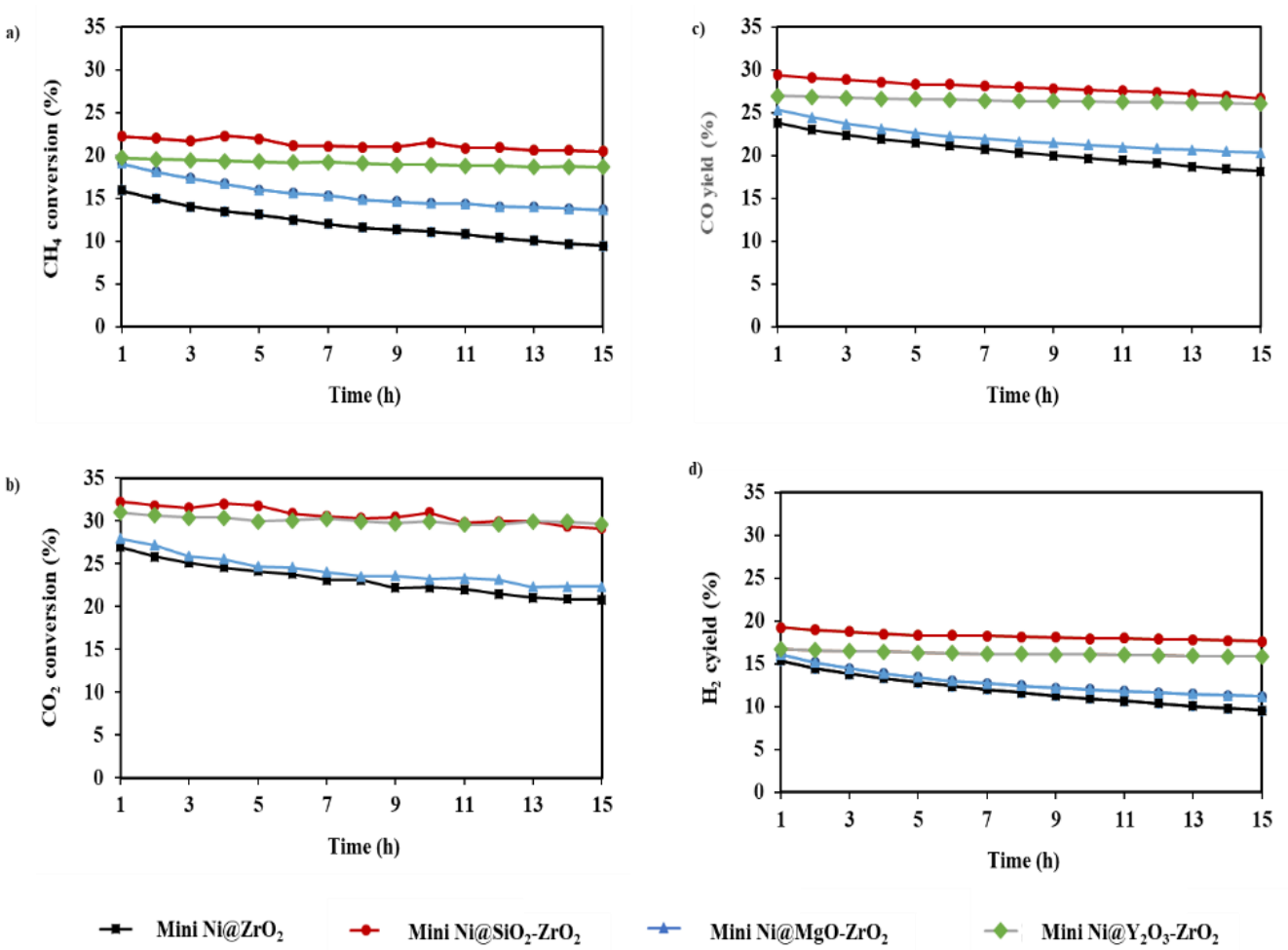


**Fig. 2-9.** DRM reactions catalyzed by Mini-series Ni@$ZrO_2$, Mini Ni/$SiO_2$–$ZrO_2$-C, Mini Ni@MgO–$ZrO_2$-C, and Mini Ni@$Y_2O_3$–$ZrO_2$-C. **a)** $CH_4$ conversions, **b)** $CO_2$ conversions, **c)** CO yields, and **d)** $H_2$ yields.

**Table 2** Reaction frequencies for 550 ℃ DRM[1)]

| Catalyst | Reaction frequency ($\times 10^3$ $s^{-1}$) | |
|---|---|---|
| | $CH_4$ | $CO_2$ |
| Mini Ni@ $ZrO_2$ | 5.7 | 11 |
| Mini Ni@$SiO_2$–$ZrO_2$-C | 9.6 | 14 |
| Mini Ni@MgO–$ZrO_2$-C | 7.0 | 11 |
| Mini Ni@$Y_2O_3$–$ZrO_2$-C | 8.4 | 13 |

1) Evaluated by conversion of reactant gas and Ni amount.

### 2–3–3. Carbon Suppression Behavior in DRM Reaction

The high catalytic activity and long-term stability of Mini Ni@$SiO_2$–$ZrO_2$-C and Mini Ni@$Y_2O_3$–$ZrO_2$-C can be ascribed to the sintering resistance behavior of the catalysts. SEM and TEM images of the spent catalysts were taken to directly clarify the carbon deposition on the catalysts (Fig. 2-10). As expected, a substantial number of carbon nanotubes (CNTs) were observed in the spent catalyst of Mini Ni@$ZrO_2$ (Fig. 2-10a) and Mini Ni@MgO–$ZrO_2$-C (Fig. 2-10c). On the other hand, in the spent catalysts

of Mini Ni@$SiO_2$–$ZrO_2$-C (Fig. 2-10b) and Mini Ni@$Y_2O_3$–$ZrO_2$-C (Fig. 2-10d), only a small number of CNT were observed.

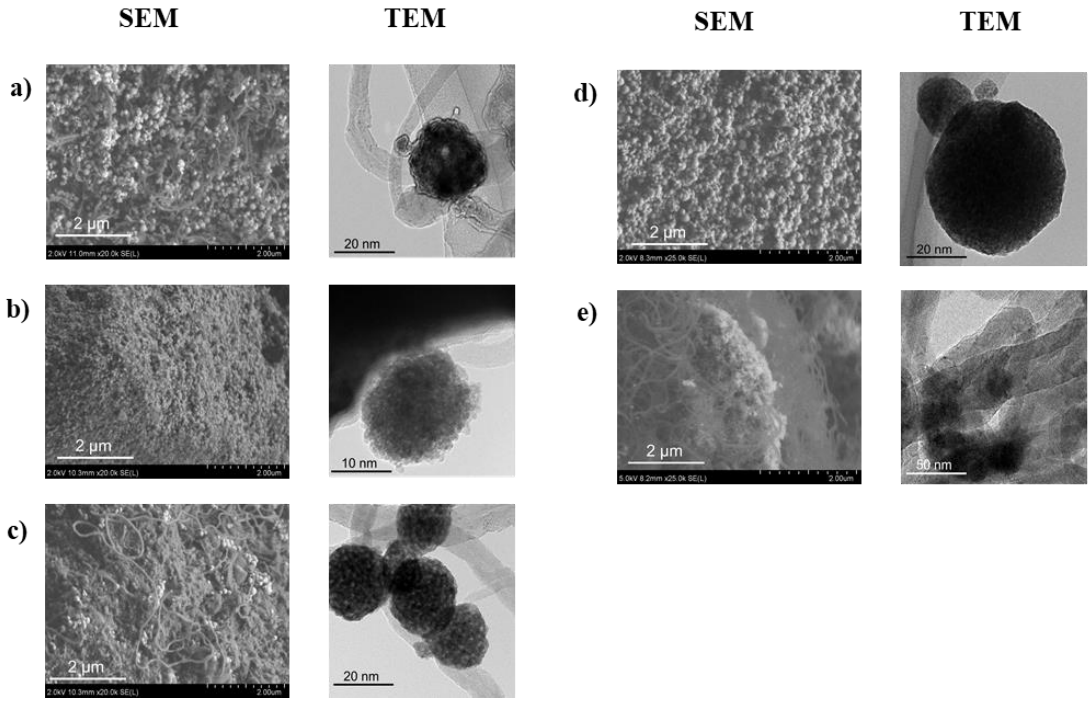


**Fig. 2-10.** SEM and TEM images of spent Ni catalysts embedded in Mini-series of Ni@$ZrO_2$-based supports. **a)** Mini Ni@$ZrO_2$, **b)** Mini Ni@$SiO_2$–$ZrO_2$-C, **c)** Mini Ni@MgO–$ZrO_2$-C, **d)** Mini Ni@$Y_2O_3$–$ZrO_2$-C, and **e)** U-Ni/$ZrO_2$

The quantity of deposited CNTs was estimated by TG analysis of the spent catalysts (Fig. 2-11). According to Fig. 2-11, weight loss of Mini Ni@$ZrO_2$ and Mini Ni@MgO–$ZrO_2$-C began around 400 °C and was nearly complete at 600 °C with weight losses corresponding to 30 and 19%, respectively. Meanwhile, in the cases of Mini Ni@$SiO_2$–$ZrO_2$-C and Mini Ni@$Y_2O_3$–$ZrO_2$-C, weight losses began at a lower temperature, around 350 °C, and were nearly completed by 550 or 600 °C with weight losses corresponding to 15 and 5%, respectively. The different decomposition initiation

temperatures of Mini-series catalyst can be attributed to the formation of different carbon species. The lower decomposition temperature predicts the formation of amorphous carbon, while the higher decomposition temperature suggests the formation of CNT [18]. The small amount of CNT in Mini $SiO_2$–$ZrO_2$-C and Mini $Y_2O_3$–$ZrO_2$-C catalysts clearly indicates that the formation of carbon species in the DRM reaction were effectively suppressed.

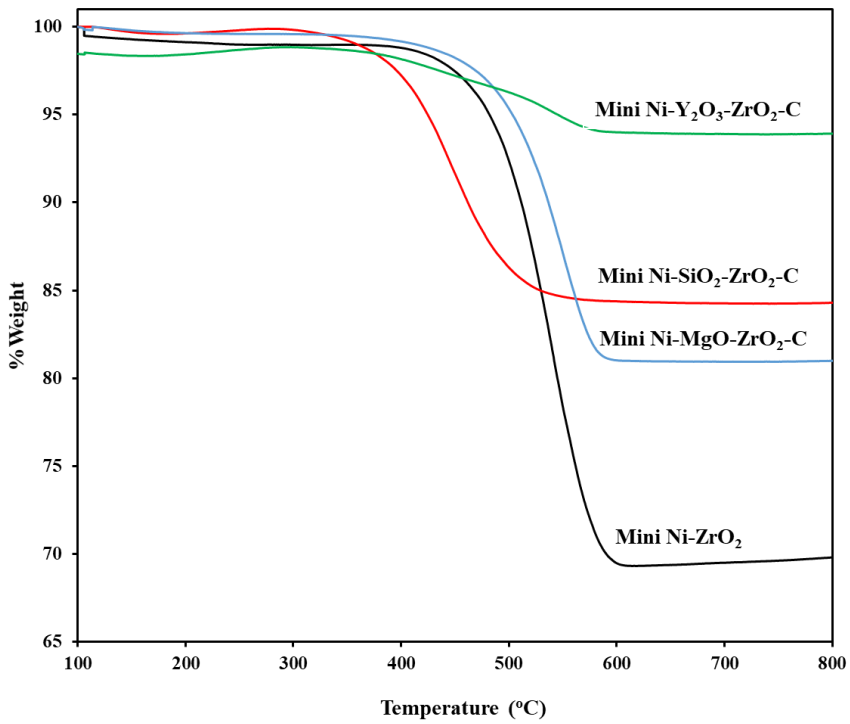


**Fig. 2-11.** TGA profiles of spent catalysts for Mini-series Ni@$ZrO_2$, Mini Ni@$SiO_2$–$ZrO_2$-C, Mini Ni@MgO–$ZrO_2$-C, and Mini Ni@$Y_2O_3$–$ZrO_2$-C.

Fig. 2-12 displays the XRD spectra of the spent catalysts. In the cases of Mini Ni@$SiO_2$–$ZrO_2$-C and Mini Ni@$Y_2O_3$–$ZrO_2$-C, almost no significant differences were observed, where the profiles left broad even after DRM. However, in the cases of Mini

Ni@$ZrO_2$ and Mini Ni@MgO–$ZrO_2$-C, sharper peaks corresponding to cubic $ZrO_2$ and cubic Ni were observed. These results clearly indicate that the sintering of the Ni particles and $ZrO_2$ primary particles were effectively suppressed in the cases of Mini Ni@$SiO_2$–$ZrO_2$-C and Mini Ni@$Y_2O_3$–$ZrO_2$-C. The confinement effect of Ni NPs and $ZrO_2$ primary particles by embedded $SiO_2$ and $Y_2O_3$ may contribute to their high catalytic performance [9].

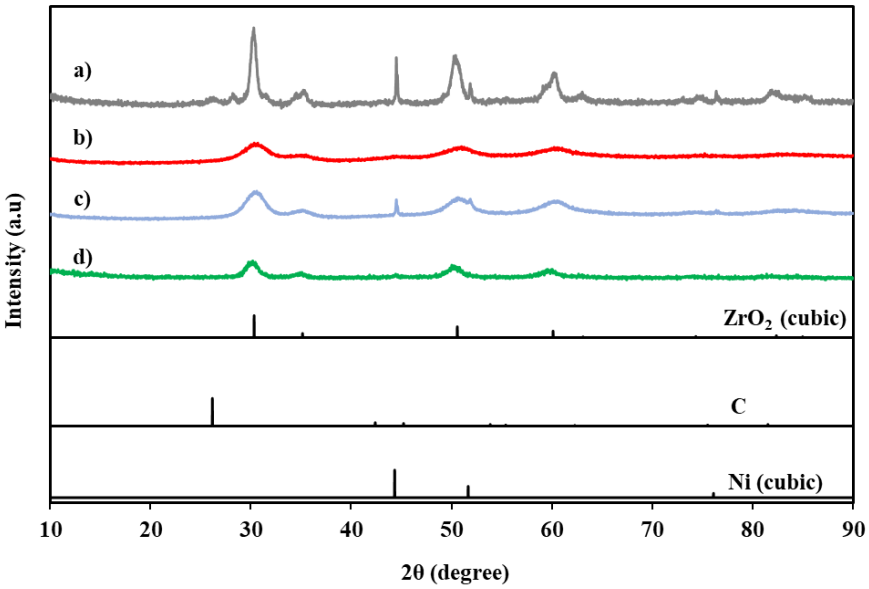


**Fig. 2-12.** XRD patterns of spent catalysts of a) Mini Ni@$ZrO_2$, b) Mini Ni@$SiO_2$-$ZrO_2$-C, c) Mini Ni@MgO–$ZrO_2$-C, and d) Mini Ni@$Y_2O_3$–$ZrO_2$-C.

## 2–4. Conclusions

Ni NP catalysts embedded in $ZrO_2$ porous spheres and $SiO_2$–$ZrO_2$, MgO–$ZrO_2$, and $Y_2O_3$–$ZrO_2$ composite porous spheres were successfully prepared by simple one-pot and single-step alcothermal reactions. By adding a small amount of water to the precursor solutions, the sizes of the porous sphere nanoparticles were reduced from 600–700 nm to 63–120 nm. To verify the catalyst activity and carbon-deposition-suppression ability of the Ni NPs, low-temperature DRM was selected as a probe reaction. The embedded Ni catalysts exhibited better catalytic activity and longer-lasting stability than the Ni impregnated commercially available $ZrO_2$ NP catalyst and Ni-impregnated $ZrO_2$ porous spherical catalyst. In addition, carbon deposition on Ni NPs was suppressed by the small $ZrO_2$ composites embedded with Ni NPs. In particular, the Ni catalyst embedded in small $SiO_2$–$ZrO_2$ porous spheres with a high specific surface area demonstrated good activity and long stability.

## References


[1] D. Xu, H. Lv, B. Liu, Encapsulation of metal nanoparticle catalysts within mesoporous zeolites and their enhanced catalytic performances: a review, Front Chem., (2018) 550–564, https://doi.org/10.3389/fchem.2018.00550.

[2] T.W. Van Deelen, C.H. Mejia, K.P. De Jong, Control of metal-support interactions in heterogeneous catalysts to enhance activity and selectivity, Nat. Catal., (2019) 955–970, https://doi.org/10.1038/s41929-019-0364-x.

[3] L.De Rogatis, M. Cargnello, V. Gombac, B. Lorenzut, T. Montini, P. Fornasiero, Embedded phases: a way to active and stable catalysts, ChemSusChem, (2010) 24–42, https://doi.org/10.1002/cssc.200900151

[4] J.C. Vedrine, Heterogeneous catalysis on metal oxides, Catalysts, (2017) 341–366, https://doi.org/10.3390/catal7110341.

[5] J. Liu, Q. Ji, T. Imai, K. Ariga, H. Abe, Sintering-resistant nanoparticles in wide-mouthed compartments for sustained catalytic performance, Sci Rep., (2017) 41773, https://doi.org/10.1038/srep41773.

[6] S. Liu, W. Xu, Y. Niu, B. Zhang, L. Zheng, W. Liu, L. Li, J. Wang, Ultrastable Au nanoparticles on titania through an encapsulation strategy under oxidative atmosphere, Nat. Commun., (2019) 5790–5799, https://doi.org/10.1038/s41467-019-13755-5.

[7] X. Zou, S. Chen, Q. Wang, X. Gao, J. Li, L. Li, Z. Wei, Leaching and sintering-resistant hollow or structurally ordered intermetallic PtFe alloy catalyst for oxygen reduction reaction, Nanoscale, (2019) 20115–20122, http://dx.doi.org/10.1039/C9NR06698E.

[8] R.K. Parsapur, S. Chatterjee, K. Huang, The insignificant role of dry reforming of methane in $CO_2$ emission relief, ACS Energy Lett., (2020) 2881–2885, https://doi.org/10.1021/acsenergylett.0c01635.

[9] W. Liu, L. Li, X. Zhang, Z. Wang, X. Wang, H. Peng, Design of Ni-$ZrO_2$@$SiO_2$ catalyst with ultra-high sintering and coking resistance for dry reforming of methane to prepare syngas, J. $CO_2$ Util., (2018) 297–307, https://doi.org/10.1016/j.jcou.2018.08.003.

[10] H. Peng, X. Zhang, X. Han, X. You, S. Lin, H. Chen, W. Liu, X. Wang, N. Zhang, Z. Wang, P. Wu, H. Zhu, S. Dai, Catalysts in coronas: a surface spatial confinement strategy for high-performance catalysts in methane dry reforming. ACS Catal., (2019) 9072–9080, https://doi.org/10.1021/acscatal.9b00968.

[11] S. Lin, J. Wang, Y. Mi, S. Yang, Z. Wang, W. Liu, D. Wu, H. Peng, Trifunctional strategy for the design and synthesis of a Ni-$CeO_2$@$SiO_2$ catalyst with remarkable low-temperature sintering and coking resistance for methane dry reforming, Chinese J. Catal., (2021) 1808–1820, https://doi.org/10.1016/S1872-2067(21)63789-0.

[12] W. Liu, L. Li, S. Lin, Y. Luo, Z. Bao, Y. Mao, K. Li, D. Wu, H. Peng, Confined Ni-In intermetallic alloy nanocatalyst with excellent coking resistance for methane dry reforming, J. Energy Chem., (2022) 34–47, https://doi.org/10.1016/j.jechem.2021.05.017.

[13] M.A.A. Aziz, A.A. Jalil. S. Wongsakulphasatch, D.V.N. Vo, Understanding the role of surface basic sites of catalysts in $CO_2$ activation in dry reforming of methane: A short review, Catal. Sci Technol., (2020) 35–45, http://dx.doi.org/10.1039/C9CY01519A.

[14] X. Gao, Z. Ge, G. Zhu, Z. Wang, J. Ashok, S. Kawi, Anti-coking and anti-sintering $Ni/Al_2O_3$ catalysts in the dry reforming of methane: recent progress and prospects, Catalysts, (2021) 1003–1021, https://doi.org/10.3390/catal11081003.

[15] Y. Tanaka, H. Usui, Y. Domi, M. Ohtani, K. Kobiro, and H. Sakaguchi, Mesoporous spherical aggregates consisted of Nb-doped anatase $TiO_2$ nanoparticles for Li and Na storage materials, ACS Appl Energy Mater., **(**2019) 636–643, https://doi.org/ 10.1021/acsaem.8b01656.

[16] S. Biswas, A. Pal, T. Pal, Supported metal and metal oxide particles with proximity effect for catalysis, RCS Adv., (2020) 35449–35472, http://dx.doi.org/10.1039/D0RA06168A.

[17] Y Wang, L Yao, Y Wang, S Wang, Q Zhao, D Mao, C. Hu, Low-temperature catalytic $CO_2$ dry reforming of methane on Ni-Si/$ZrO_2$ catalyst, ACS Catalyst, (2018) 6495–6506, https://doi.org/10.1021/acscatal.8b00584.

[18] N.D. Charisiou, S.L. Douvartzides, G.I. Siakavelas, L. Tzounis, V. Sebastian, V. Stolojan, S.J. Hinder, M.A. Baker, K. Polychronopoulou, M.A. Goula, The relationship between reaction temperature and carbon deposition on nickel catalysts based on $Al_2O_3$, $ZrO_2$ or $SiO_2$ supports during the biogas dry reforming reaction, Catalysis, (2019) 676-698, https://doi.org/10.3390/catal9080676.

# Chapter 3

## Nitrilethermal Synthesis of $Ceo_2$-Based Composite Nanoparticles as Ru and Pd Catalyst Supports for $CO_2$ Methanation and $CH_4$ Oxidation

### 3–1. Introduction

Nowadays, materials synthesis using high-temperature and high-pressure reaction media such as water and organic solvents is becoming a new trend in many research and industrial fields [1]. In supercritical conditions, water exhibits good solubility to inorganic materials. For this reason, materials synthesis using water in high-temperature and high-pressure reaction media (hydrothermal method) has been widely used to prepare many types of inorganic materials [2,3]. However, the rapidity of hydrothermal reactions makes it challenging to control product crystal size, crystallinity, and aggregation of the materials [4]. On the other hand, solvothermal synthesis to obtain inorganic materials using organic solvents under high-temperature conditions has grown in popularity [5]. As a result, much effort has been put into exploring inorganic materials synthesis using solvothermal method.

Among various kinds of nanomaterials, nano-sized metal oxides show various attractive features, such as semi-conductivity, thermal stability, and abundance oxygen vacancies [6]. Solvothermal methods have been used to obtain a number of nano-sized metal oxides.Previously, our group has been developing a one-pot and single-step solvothermal approach affording submicron-sized, monodisperse, and porous metal oxide assemblies has been developed [7]. Various nanosized metal oxides and their composites, for instance, solid and/or hollow $SiO_2$, $TiO_2$, ZnO, $ZrO_2$, and $CeO_2$ with large surface

areas were successfully obtained by employing supercritical alcohols (methanol and ethanol) [8]. The obtained $TiO_2$ MARIMO exhibited an ultrafine surface concave-convex structure and was applied as a catalyst support to prevent sintering of dispersed Au nanoparticles [9]. Furthermore, our group have successfully prepared $Al_2O_3$–$TiO_2$ and ZnO–$TiO_2$ hollow composite MARIMOs with very large specific surface areas (250–600 $m^2/g$) [10]. In addition, Ni nanoparticle catalysts embedded in $ZrO_2$ and $ZrO_2$-composite MARIMOs (MgO–$ZrO_2$, $SiO_2$–$ZrO_2$, and $Y_2O_3$–$ZrO_2$) with specific surface areas of 167−269 $m^2/g$ were prepared by a similar one-pot and one-step solvothermal reaction in moist ethanol as mentioned in Chapter 2 [11]. When those composites were utilized as catalyst supports of Ni catalysts for dry reforming of methane at the relatively low temperature of 550 °C, the composites (especially $SiO_2$-$ZrO_2$) suppressed the carbon deposition on the catalyst metal nanoparticles, providing high catalytic activity and stability. Similarly, monodispersed $Nb_2O_5$ with high crystallinity and large surface areas (~300 $m^2/g$) [12] and $Nb_2O_5$–$TiO_2$ composite MARIMOs were prepared and applied as an anode material in lithium-ion batteries [13]. In the same manner, MgO MARIMOs have been successfully prepared [14]. To obtained MgO MARIMOs, first methanol was selected as a solvent for the solvothermal reaction of precursor solutions containing $Mg(NO_3)_2$ or $Mg(acac)_2$. However, the reaction resulted in the formation of $Mg_2O(OH)_2$ or $Mg(OH)_2$ instead of the expected MgO. It can be concluded that the formation of water was generated by the condensation of methanol at high temperatures can be a reason for the formation of the hydroxides.

On the other hand, acetonitrile is frequently used in both organic and inorganic processes due to its high polarity. Acetonitrile is a typical aprotic solvent and has a higher

polarity ($\varepsilon_r$ = 35.94) than methanol ($\varepsilon_r$ = 32.66). Acetonitrile can dissolve many inorganic and organic materials even though the lack of hydroxy group [15]. Moreover, despite being heated to high temperatures, acetonitrile never produces water due to the absence of hydroxy group. As a result, acetonitrile works well as a solvent for both inorganic and organic reactions at high temperatures. However, studies on solvothermal synthesis using acetonitrile to obtain nanosized materials are remarkably unexplored. To our best knowledge, there are two studies. Buha *et al.* synthesized $In_2O_3$ and ZnO nanoparticles with high-crystallinity through solvothermal synthesis from a precursor solution containing metal salts in acetonitrile at just 100 °C for 2 days [16]. Leubner *et al.* synthesized three significantly different benchmarks of metal-organic-frameworks in acetonitrile at 100–130 °C [17]. Morover, in the previous studies, the desired product was easily produced using acetonitrile instead of methanol as the solvent for the MgO MARIMO synthesis [13]. Acetonitrile was also used in the solvothermal reactions produceding $CeO_2$ MARIMOs with high $Ce^{3+}$ content, [18].

In this context, the acetonitrile-based solvothermal synthetic approach, which termed 'nitrilethermal' synthesis, is extended to the preparation of $CeO_2$ and $CeO_2$-based composites ($Al_2O_3$−$ZrO_2$, $SiO_2$−$CeO_2$, $Y_2O_3$−$CeO_2$, and $ZrO_2$−$CeO_2$). The properties of $CeO_2$ and $CeO_2$-based composites, especially oxygen-storage capacities, were investigated, as was their application as supports for Ru and Pd nanometal catalysts for $CO_2$ methanation and $CH_4$ oxidation, respectively.

## 3–2. Experiment

### 3–2–1. Materials

Cerium (III) nitrate hexahydrate ($Ce(NO_3)_3 \cdot 6H_2O$), zirconyl nitrate dihydrate

($ZrO(NO_3)_2 \cdot 2H_2O$), aluminum(III) nitrate nonahydrate ($Al(NO_3)_3 \cdot 9H_2O$), tetraethoxysilane ($Si(OCH_2CH_3)_4$, TEOS), yttrium(III) nitrate n-hydrate ($Y(NO_3)_3 \cdot nH_2O$), and palladium(III) acetate ($Pd(OCOCH_3)_3$) were purchased from Fujifilm Wako Pure Chemical Corporation. Acetonitrile, tris(2,4-pentanedionato)-ruthenium(III) ($Ru(acac)_3$) and triethylene glycol were purchased from Tokyo Chemical Industry Co., Ltd. Standard material JRC-CEO-5 $CeO_2$ (abbreviated as $CeO_2$-J) was obtained from Daiichi Kigenso Kagaku Kogyo Co., Ltd. All reagents were used without further purification.

### 3–2–2. Preparation method

#### 3–2–2–1. Preparation of $CeO_2$-based composites

A precursor solution containing $Ce(NO_3)_3 \cdot 6H_2O$ (5.45 g, 12.6 mmol), $ZrO(NO_3)_2 \cdot 2H_2O$ (378 mg, 1.41 mmol), and triethylene glycol (66.7 g, 444 mmol) in a mixed solvent of acetonitrile (126 mL) and ethanol (14 mL) was transferred to an SUS-316 stainless-steel reactor (MMS-5000, OM LAB-TECH Co., Ltd.) and the solution was heated at 300 °C for 10 min. After cooling, the reaction mixture was centrifuged and the supernatant was decanted off. The precipitate was washed with methanol several times. The obtained solid was dried at 50 °C under vacuum to give the powdery composite product $ZrO_2$–$CeO_2$, which was labeled $ZrO_2$–$CeO_2$-C (C represents composite). Similar procedures using $Al(NO_3)_3 \cdot 9H_2O$ (522 mg, 1.39 mmol), TEOS (296 mL, 1.42 mmol), and $Y(NO_3)_2 \cdot nH_2O$ (537 mg, 1.40 mmol; were calculated assuming the 6 hydrate) were employed to obtain the $Al_2O_3$–$CeO_2$ composite, the $SiO_2$–$CeO_2$ composite, and the $Y_2O_3$–$CeO_2$ composite, respectively, which were abbreviated as $Al_2O_3$–$CeO_2$-C, $SiO_2$–$CeO_2$-C, and $Y_2O_3$–$CeO_2$-C, respectively. The atomic ratios of Al/Ce, Si/Ce, Y/Ce, and

Zr/Ce in the precursor solutions were 1:9.

### 3–2–2–2. Preparation of Pd and Ru catalysts supported on $CeO_2$-based composites

Pd catalysts supported on $CeO_2$ porous spheres ($CeO_2$-M; M represents MARIMO) were prepared by the impregnation method [19]. A solution of $Pd(OCOCH_3)_2$ (10.3 mg, 0.0459 mmol) in 5 mL of acetonitrile was added to a dispersion of 500 mg $CeO_2$-M in 5 mL of acetonitrile. The dispersion was mixed well using a planetary centrifugal mixer (Thinky AR-100) for 2 h until a dry powder was obtained. The powder was further dried in air at 110 °C for 2 h and then calcined in air at 300 °C for 2 h to produce the impregnated Pd catalyst (denoted as Pd/$CeO_2$). Using the same procedure, Pd/$Al_2O_3$–$CeO_2$-C, Pd/$SiO_2$–$CeO_2$-C, Pd/$Y_2O_3$–$CeO_2$-C, Pd/$ZrO_2$–$CeO_2$-C, and Pd/$CeO_2$-J were prepared. The Pd contents of the impregnated catalysts were all ~1 wt%.

Using a similar technique, 3 wt%-Ru catalysts supported on $CeO_2$-based composites were prepared. $Ru(acac)_3$ was used as the Ru source in the preparations. The catalysts obtained from $CeO_2$-M, $Al_2O_3$–$CeO_2$-C, $SiO_2$–$CeO_2$-C, $Y_2O_3$–$CeO_2$-C, $ZrO_2$–$CeO_2$-C, and commercially available $CeO_2$-J were labeled Ru/$CeO_2$, Ru/$Al_2O_3$–$CeO_2$, Ru/$SiO_2$–$CeO_2$, Ru/$Y_2O_3$–$CeO_2$, Ru/$ZrO_2$–$CeO_2$, and Ru/$CeO_2$-J, respectively.

### 3–2–3. Characterization

#### 3–2–3–1. General

Transmission electron microscopy (TEM) images were obtained using a JEOL JEM-2100F microscope. Energy-dispersive X-ray (EDX) spectroscopy was performed using an Oxford INCA X-Max 80 EDX spectrometer unit in combination with the TEM

instrument. Scanning electron microscopy (SEM) images were obtained using a Hitachi SU8020 FE-SEM. Elemental analysis was carried out on a Malvern Panalytical Epsilon 1 X-ray fluorescence (XRF) spectrometer. Nitrogen adsorption/desorption experiments were conducted using a MicrotracBEL BELSORP mini II instrument. Specific surface areas were calculated by the Brunauer–Emmett–Teller (BET) method using the obtained nitrogen adsorption-desorption isotherms. The crystalline phases of the composites were identified by X-ray diffraction (XRD) using a Rigaku SmartLab SE diffractometer with Ni-filtered Cu-Kα radiation (X-ray wavelength: 1.5418 Å). The data were recorded over the $2\theta$ range 10–90 °. X-ray photoelectron spectroscopy (XPS) was performed on a Shimadzu/Kratos Analytical AXIS-HS instrument.

### 3–2–3–2. $O_2$ pulse measurements

The $CeO_2$-based composites were calcined in air at 300 °C for 2 h to remove organic residues. Then, the calcined composites were reduced in $H_2$/He = 1/9 (*v*/*v*) at 30 sccm and 400 °C for 1 h. $O_2$ pulse experiments were performed in $O_2$/He = 1/9 (*v*/*v*) at 30 sccm and 400 °C. The measurements were repeated three times. For the non-calcined composites (as-prepared), the $H_2$/He reduction step was omitted.

### 3–2–4. Catalytic activity

### 3–2–4–1. $CO_2$ methanation

The catalytic activities of the composite-supported metals for $CO_2$ methanation were measured using a MicrotracBEL BELCAT II flow-type reactor. First, the catalyst (50 mg) was set in a quartz tubular reactor (inner diameter = 7.5 mm) and fixed with quartz wool on both sides. Then, the catalyst was pretreated under 50 mL/min of $H_2$ gas flow at

300 °C for 3 h. The $CO_2$ methanation reaction was carried out by feeding a mixture of 5% $CO_2$, 20% $H_2$, and 75% Ar at a total gas flow rate of 40 mL/min at 100–500 °C. The gaseous products were determined with a mass detector unit (MicrotracBEL BELMASS) fitted to the MicrotracBEL BELCAT II flow-type reactor.

### 3–2–4–1. Methane oxidation

The catalyst (50 mg) was loaded into a quartz tubular reactor and fixed with quartz wool on both sides. Then, the catalyst was purged under Ar at 100 mL/min and 150 °C for 1 h. Methane oxidation was conducted at 100 mL/min and 50–600 °C using a mixture of 2% $CH_4$, 8% $O_2$, and 90% Ar. The gaseous products were determined with the same mass detector.

## 3–3. Results and discussion

### 3–3–1. Synthesis of $CeO_2$-based composites

Previously, nitrilethermal synthesis was employed to obtain $CeO_2$-M [18]. First, the combination of a protic solvent, methanol, and an additive, formic acid, acetic acid, or *o*-phthalic acid, to obtain $CeO_2$-M was tested. However, $CeO_2$ aggregates or agglomerates with irregular sizes and shapes were produced in those combinations. On the other hand, the combination of an aprotic solvent, acetonitrile, and triethylene glycol resulted in almost perfect spherical monodispersed $CeO_2$ MARIMO [20]. Additionally, $CeO_2$ MARIMO with significant amount of $Ce^{3+}$ $Ce^{3+}$/Ce atomic ratio = 0.574) in comparison to standard $CeO_2$ (ca. 0.2) were successfully obtained.

Taking the versatility of acetonitrile into the solvothermal synthesis method, a solvothermal synthesis method using acetonitile as a solvent termed “nitrilethermal” has been developed to obtain $CeO_2$ composites or to embed noble metal into $CeO_2$ composites. In the first attempt to embed noble metal into $CeO_2$ composites, Pd along with additional oxides such as $SiO_2$, $Al_2O_3$, $ZrO_2$, and $Y_2O_3$ was combine into $CeO_2$ MARIMO. A precursor solution containing $Pd(OCOCH_3)_2$ as a metal source and $Ce(NO_3)_3{\cdot}6H_2O$ mixed with TEOS, $ZrO(NO_3)_2{\cdot}2H_2O$, $Al(NO_3)_3{\cdot}9H_2O$, or $Y(NO_3)_3{\cdot}nH_2O$ in acetonitrile was heated from room temperature to 300 °C and the temperature was maintained for 10 min. The grayish powdery products were successfully obtained from this process. According to TEM analysis (Fig.3-1), Pd@$ZrO_2$–$CeO_2$-C and Pd@$Y_2O_3$–$CeO_2$ showed monodispersed spherical morphologies. Conversely,

Pd@$SiO_2$–$CeO_2$-C and Pd@$Al_2O_3$–$CeO_2$-C showed an aggregation of primary particles.

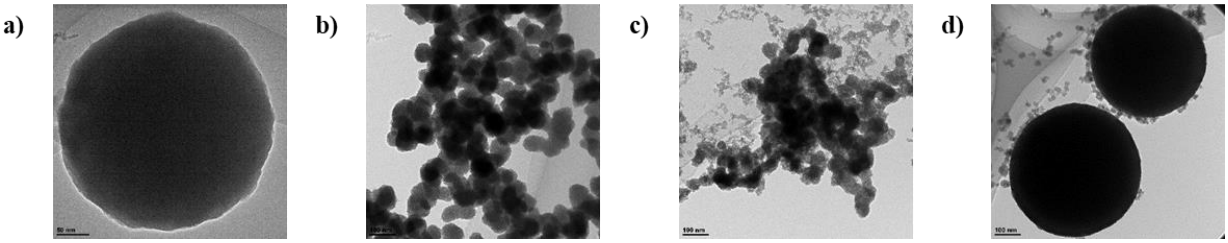


**Fig. 3-1.** TEM images of Pd@$CeO_2$-based composites. **a)** Pd@$ZrO_2$–$CeO_2$-C, **b)** Pd@$SiO_2$–$CeO_2$-C, **c)** Pd@$Al_2O_3$–$CeO_2$-C, and **d)** Pd@$Y_2O_3$–$CeO_2$-C.

However, SEM/EDX and TEM/EDX analysis showed that Pd was agglomerated and not thoroughly dispersed well in all $CeO_2$ composites. From this point, the second attempt was dedicated to impregnate noble metal particles using a two-step method. Porous $CeO_2$-M and composites were synthesized by the nitrilethermal method followed by using the impregnation of metal catalysts.

To obtained $CeO_2$-based composites for catalyst supports by the nitrilethermal method, $SiO_2$, $Al_2O_3$, $ZrO_2$, or $Y_2O_3$ were selected and mixed into $CeO_2$ MARIMO. By mixing additional oxides, surface extension can be expected in of $SiO_2$–$CeO_2$-C and $Al_2O_3$–$CeO_2$-C composites; and solid solution formation in the cases of $ZrO_2$–$CeO_2$-C and $Y_2O_3$–$CeO_2$-C composites can be predicted. For this purpose, all reagents should be dissolved in solvents to produce homogeneous precursor solutions. In this case, $Ce(NO_3)_3 \cdot 6H_2O$ and TEOS were easily dissolved in acetonitrile, while the solubility of $ZrO(NO_3)_2 \cdot 2H_2O$, $Al(NO_3)_3 \cdot 9H_2O$, and $Y(NO_3)_3 \cdot nH_2O$ to acetonitrile was relatively limited. Thus, a small amount of ethanol (14 mL) was added to acetonitrile (126 mL).

A simple preparation method was implemented in this nitrilethermal method. First, a precursor solution containing $Ce(NO_3)_3 \cdot 6H_2O$ and either TEOS, $ZrO(NO_3)_2 \cdot 2H_2O$,

$Al(NO_3)_3 \cdot 9H_2O$, or $Y(NO_3)_3 \cdot nH_2O$; and triethylene glycol were prepared and heated up to 300 °C in a pressure vessel. The obtained composites are referred to as $ZrO_2$–$CeO_2$-C, $SiO_2$–$CeO_2$-C, $Al_2O_3$–$CeO_2$-C, and $Y_2O_3$–$CeO_2$-C, respectively.

### 3–3–2. General properties of the $CeO_2$-based composites

#### 3–3–2–1. Morphology analysis

SEM and TEM images of the $CeO_2$ based composites were shown in Fig. 3-2. $ZrO_2$–$CeO_2$-C and $Y_2O_3$–$CeO_2$-C exhibited relatively spherical morphology similar to $CeO_2$-M with the particle size of around 523–1120 nm. However, $SiO_2$–$CeO_2$-C and $Al_2O_3$–$CeO_2$-C showed aggregates of tiny primary particles. The number of primary particles assembled in the $CeO_2$ composites affects the size of the secondary particles. the physical and chemical properties of $Al_2O_3$ and $SiO_2$ are significantly different from those of $CeO_2$, may explain the small proportions of the secondary particles in the $Al_2O_3$-$CeO_2$-C and $SiO_2$-$CeO_2$-C.

#### 3–3–2–2. Element Analysis

To assess the dispersion of additional elements in the $CeO_2$-based composites, STEM-EDX and XRF analyses were performed. **Table 1** summarizes the amounts of the additional elements in the $CeO_2$–based composites evaluated by STEM/EDX and XRF analysis. The added metal oxides are uniformly dispersed throughout the materials in all STEM/EDX mapping (Fig. 3-2). STEM/EDX analysis represents the dispersion of additional elements ranging from 5.9–10.3 at%. XRF analysis shows the dispersion of additional elements ranging from 8.4–11.9 at% as a percentage of the total

**Table 1** Secondary particle sizes, specific surface areas, and elemental contents of the $CeO_2$-based supports.

| Material[1)] | Secondary particle size[2)] (nm) | Specific surface area[3)] ($m^2/g$) | Elemental content[4)] | | | | |
|---|---|---|---|---|---|---|---|
| | | | Zr | Si | Al | Y | Ce |
| $CeO_2$-M | 440±40 | 152 | – | – | – | – | 100 |
| $ZrO_2$-$CeO_2$-C | 1120±10 | 102 | 8.7 (8.4) | – | – | – | 91.3 (92.4) |
| $SiO_2$-$CeO_2$-C | 43±20 | 124 | – | 9.2 (8.9) | – | – | 90.8 (94.4) |
| $Al_2O_3$-$CeO_2$-C | 83±20 | 110 | – | – | 5.9 (11.9) | – | 94.1 (88.1) |
| $Y_2O_3$-$CeO_2$-C | 532±86 | 101 | – | – | – | 10.3 (9.8) | 89.7 (90.2) |

1) As-prepared.

2) Evaluated from SEM images of at least 100 particles.

3) Brunauer–Emmett–Teller method.

4) at% values for Zr, Si, Al, and Y to the total amount of Ce by STEM/EDX analysis. Results from X-ray fluorescence analysis are given in parentheses.

amounts of corresponding additional elements to that of Ce. These results are comparable to those of the additional elements in the precursor solutions.

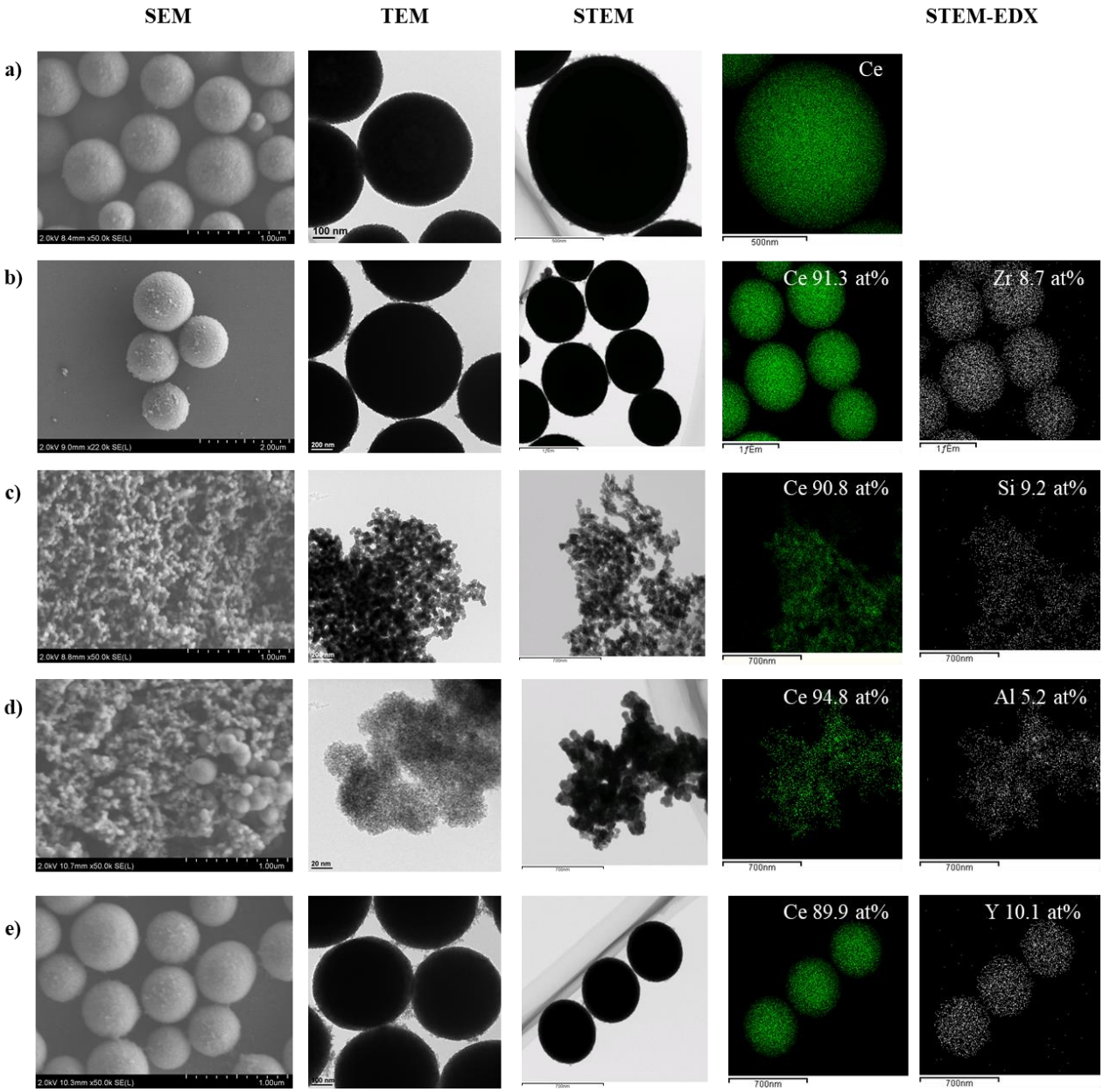


**Fig. 3-2.** SEM, TEM, STEM, and STEM-EDX images of the $CeO_2$-based composites. **a)** $CeO_2$-M, **b)** $ZrO_2$–$CeO_2$-C, **c)** $SiO_2$–$CeO_2$-C, **d)** $Al_2O_3$–$CeO_2$-C, and **e)** $Y_2O_3$–$CeO_2$-C.

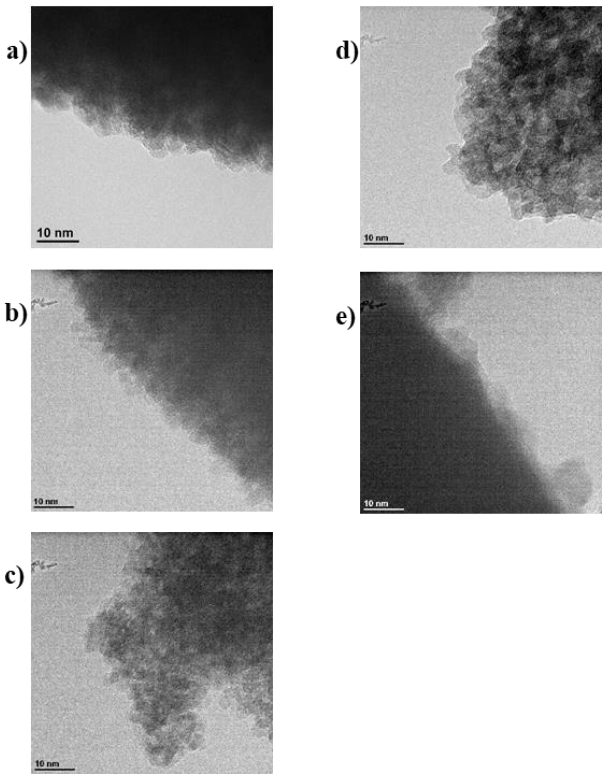


**Fig. 3-3.** HRTEM images of the $CeO_2$-based composites. **a)** $CeO_2$-M, **b)** $ZrO_2$–$CeO_2$-C, **c)** $SiO_2$–$CeO_2$-C, **d)** $Al_2O_3$–$CeO_2$-C, and **e)** $Y_2O_3$–$CeO_2$-C.

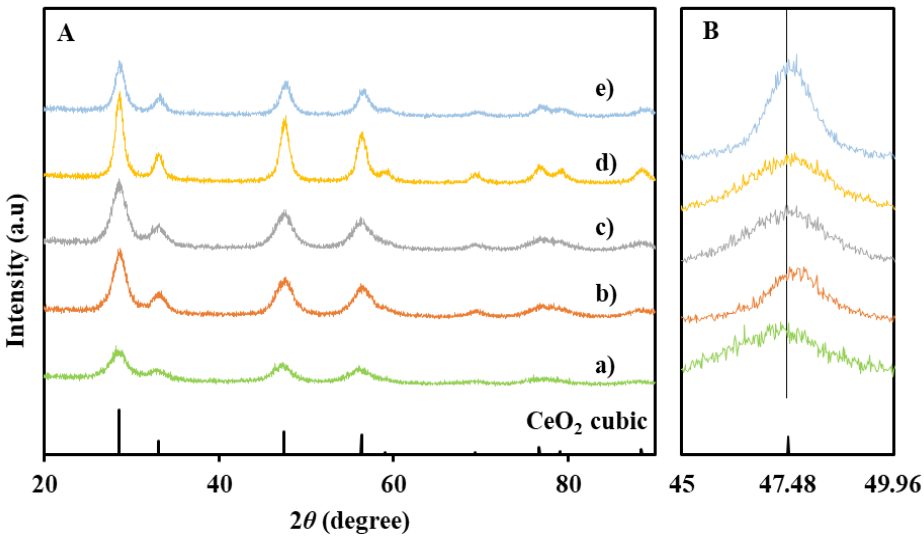


**Fig. 3-4.** XRD patterns of the $CeO_2$-based composites. **(A) a)** $CeO_2$-M, **b)** $ZrO_2$–$CeO_2$-C, **c)** $SiO_2$–$CeO_2$-C, **d)** $Al_2O_3$–$CeO_2$-C, and **e)** $Y_2O_3$–$CeO_2$-C. **(B)** Expansion of the (220) peaks.

### 3–3–2–3. Specific surface area

The specific surface areas of $CeO_2$-based composites are relatively high ranging from 100 to 150 $m^2/g$. The specific surface areas of the $CeO_2$-based composites are summarized in Table 1. In addition, $ZrO_2$–$CeO_2$-C and $Y_2O_3$–$CeO_2$-C show nano-concave-convex structures, which have been shown to suppress the migration of well-dispersed nanometal particles on their surfaces (Fig. 3-3) [7].

## 3–3–3. Physical properties of the $CeO_2$-based composites

### 3–3–3–1. XRD spectra

Fig. 3-4 displays the XRD spectra of the $CeO_2$-based composites. Broad peaks that are related to the cubic $CeO_2$ crystal phase can be seen in all the composites. The details about of physical characteristics of $CeO_2$-based composites are provided by the expansion of the (220) peak. The increasement in the lattice parameter estimated by the peak of $CeO_2$ (220) facet is represented by a slight shift from the initial $CeO_2$-M position (47.48°). This may be caused by a high concentration of $Ce^{3+}$ in the $CeO_2$ lattice with larger ionic radius (0.13 nm) than that of $Ce^{4+}$ (0.11 nm) as explained in the prior study [16].

$Al_2O_3$–$CeO_2$-C, $SiO_2$–$CeO_2$-C, $Y_2O_3$–$CeO_2$-C, and $ZrO_2$–$CeO_2$-C showed similar peak positions ($Al_2O_3$–$CeO_2$-C, $SiO_2$–$CeO_2$-C, and $Y_2O_3$–$CeO_2$-C) or slightly higher one ($ZrO_2$–$CeO_2$-C) compared to pure $CeO_2$ (47.48°). The similar peak positions of $CeO_2$-based composites to that of pure $CeO_2$ indicate that $Ce^{4+}$ with small ionic radius (0.11 nm) in the $CeO_2$ composite lattices are replaced by the smaller ionic radius of additional oxides, such as $Zr^{4+}$ (0.09 nm), $Si^{4+}$ (0.03 nm), $Al^{3+}$ (0.04 nm), or $Y^{3+}$ (0.03 nm). respectively. The corresponding solid solutions of $ZrO_2$ and $Y_2O_3$ are easily formed. However, because

of the different crystal lattice between $CeO_2$, $SiO_2$, and/or $Al_2O_3$, the formation of solid solutions from these components is quite challenging. A high-temperature reaction at 300 °C during the synthesis process, leaves the possibility that a small amount of Si or Al may exist in the $CeO_2$ crystal lattice causing a crystal strain. Additionally, the quenching process in an ice bath may stop the reaction and stabilize the crystal lattice.

### 3–3–3–2. XPS spectra

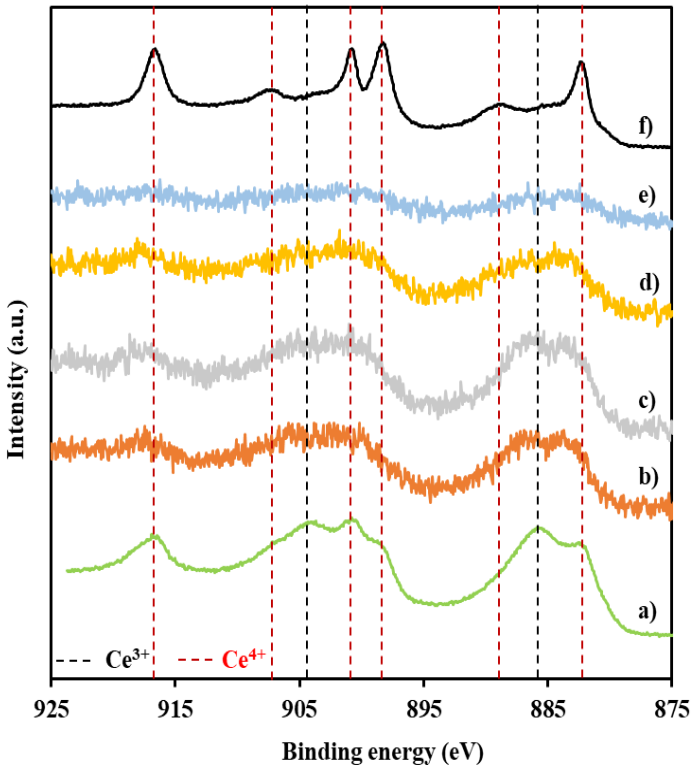


**Fig. 3-5.** XPS spectra of **a)** $CeO_2$-M, **b)** $ZrO_2$–$CeO_2$-C, **c)** $SiO_2$–$CeO_2$-C, **d)** $Al_2O_3$–$CeO_2$-C, **e)** $Y_2O_3$–$CeO_2$-C, and **f)** $CeO_2$-J. The profiles of **a)** and **f)** were taken from reference 16.

The $Ce^{3+}/Ce^{4+}$ ratios in the $CeO_2$ composites were estimated by XPS spectra (Fig. 3-5). $CeO_2$-M has a distinctive profile with rich in $Ce^{3+}$ species. Similar XPS profiles to those of $CeO_2$-M can also be seen in $ZrO_2$–$CeO_2$-C, $SiO_2$–$CeO_2$-C, $Al_2O_3$–$CeO_2$-C, and $Y_2O_3$–$CeO_2$-C. Since the broadening signals plotted, it is quite difficult to make a firm conclusion because of the broadening signals. However, the result clearly indicates that these composites have rich $Ce^{3+}$ in crystal lattices.

### 3–3–3–3. Oxygen-storage capacities of $CeO_2$-based composites

$CeO_2$ is well known for its high oxygen storage capacity (OSC) originated from high concentration of $Ce^{3+}$, which facilitates the $Ce^{3+}/Ce^{4+}$ redox cycle and gives good catalytic performance in oxidation. In a previous study, it was shown that the $Ce^{3+}/Ce^{4+}$ ratio of nitrilethermally produced $CeO_2$-M reaches 0.574, indicating the presence of a significant amount of $Ce^{3+}$ in the crystals [16]. The $CeO_2$-based composites' XPS spectra (Fig. 3-5) clearly indicate the presence of $Ce^{3+}$ ions in the crystals, which features high OSC values.

To eliminate organic residues and prevent the primary $CeO_2$ particles from sintering, the composites were first calcined in air for two hours at a relatively moderate temperature of 300 °C. During this process, a portion of the $Ce^{3+}$ in the $CeO_2$ was oxidized to $Ce^{4+}$. Then, the calcined $Ce^{4+}$-rich composites were reduced to $Ce^{3+}$ in $H_2$ at the comparatively low temperature of 400 °C. An $O_2$ pulse experiment followed by $H_2$ reduction was repeated three times.

Fig. 3-6 represents the result of OSC through the $O_2$ pulse measurements. In contrast to $CeO_2$-J, the $CeO_2$-based composites ($CeO_2$-M, $ZrO_2$–$CeO_2$-C, $SiO_2$–$CeO_2$-C, $Al_2O_3$–

$CeO_2$-C, and $Y_2O_3$-$CeO_2$-C) exhibited larger OSC values. For the initial measurement, $SiO_2$-$CeO_2$-C had the highest OSC value (758 mol-O/g) of the group. The insufficient reduction of $Ce^{4+}$ by $H_2$ at the low temperature of 400 °C can be attributed to the composites' OSC values declining cycle by cycle. $Ce^{4+}$ is often reduced at temperatures higher than 800 °C [21]. The composites, however, can be reduced at a significantly lower temperature of 400 °C, indicating that the $CeO_2$-based composites are featured by their ease of reduction characteristic. After the third cycle, the OSC values of $CeO_2$-M, $ZrO_2$–$CeO_2$-C, $SiO_2$–$CeO_2$-C, $Al_2O_3$–$CeO_2$-C, $Y_2O_3$–$CeO_2$-C, and $CeO_2$-J were 260, 556, 342, 436, 159, and 112 mol-O/g, respectively.

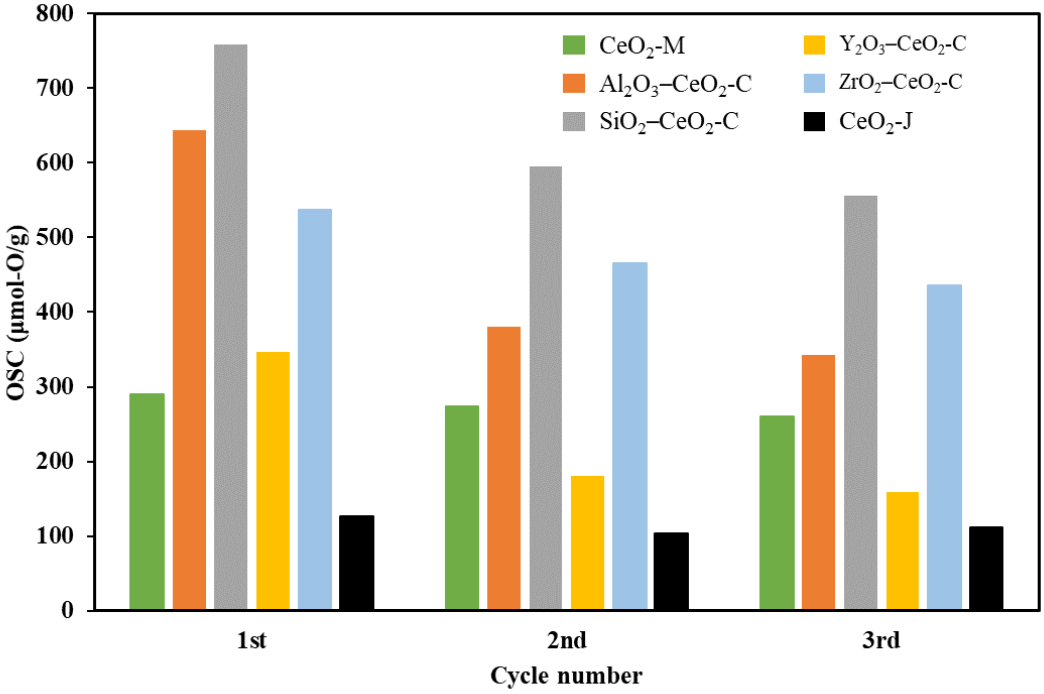


**Fig. 3-6.** OSCs of $CeO_2$-M, $ZrO_2$–$CeO_2$-C, $SiO_2$–$CeO_2$-C, $Al_2O_3$–$CeO_2$-C, $Y_2O_3$–$CeO_2$-C, and J-$CeO_2$ measured at 400 °C over three cycles.

The OSC of $CeO_2$-based composites with and without $H_2$ reduction(as-calcined) is shown in Fig. 3-7. The ratios of $OSC_{Al_2O_3–CeO_2-C}/OSC_{CeO_2-M}$ (2.6), $OSC_{SiO_2–CeO_2-}$

$_{C}$/$OSC_{CeO_2\text{-}M}$ (4.2), and $OSC_{Y_2O_3\text{–}CeO_2\text{-}C}$/$OSC_{CeO_2\text{-}M}$ (0.6) in the absence of $H_2$ reduction are higher than those in the presence of $H_2$ reduction, indicating that the proportions of $Ce^{3+}$ in the calcined $CeO_2$-based composites are higher. As a result, the $SiO_2$–$CeO_2$-C, $Al_2O_3$–$CeO_2$-C, and $Y_2O_3$–$CeO_2$-C composites are $Ce^{3+}$-rich, even the as-calcined samples. Furthermore, in the case of $ZrO_2$–$CeO_2$-C, the OSC value is highly enhanced by $H_2$ reduction, indicating its ready $Ce^{3+}/Ce^{4+}$ redox cycling.

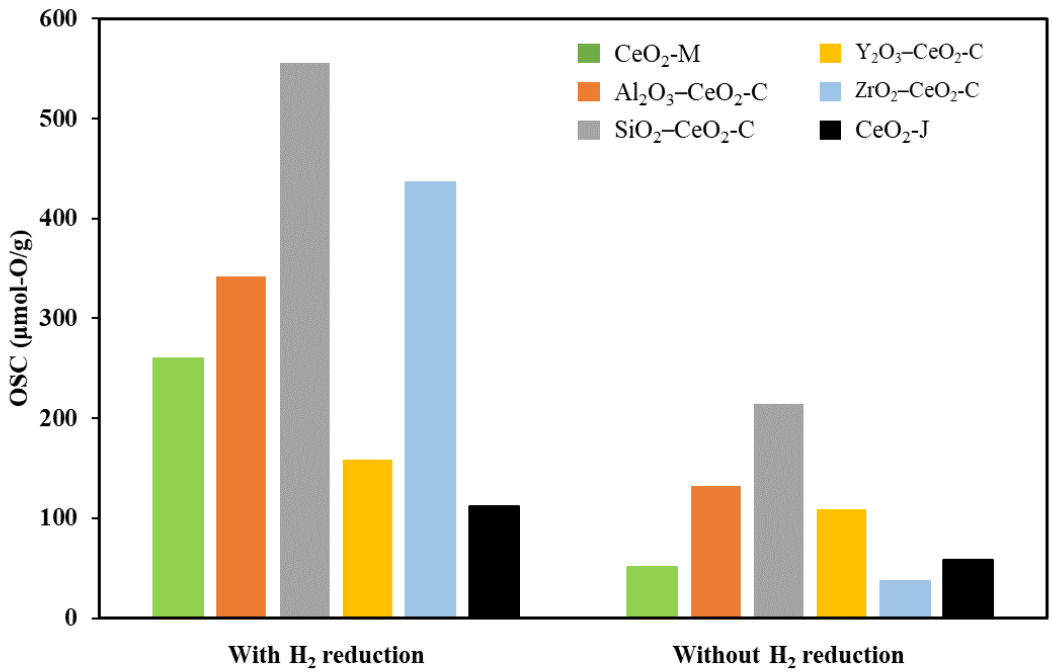


**Fig. 3-7.** OSCs of $CeO_2$-M, $ZrO_2$–$CeO_2$-C, $SiO_2$–$CeO_2$-C, $Al_2O_3$–$CeO_2$-C, $Y_2O_3$–$CeO_2$-C, and $CeO_2$-J with $H_2$ reduction (the same as that for the 3rd cycle in Fig. 3-6) and without $H_2$ reduction.

### 3–3–4. Application of $CeO_2$-based composites to catalyst supports

The composites made of $CeO_2$ were used as catalyst supports for nanometal catalysts. Ru and Pd were selected as nanometal catalysts for $CO_2$ methanation and $CH_4$

oxidation, respectively. Both $CO_2$ methanation and $CH_4$ oxidation are essential reactions for environmental preservation [22].

$$CO_2 + 4H_2 \rightarrow CH_4 + H_2O, \Delta H^0 = -165 \text{ kJ mol}^{-1} \quad (2)$$

$$CH_4 + 2O_2 \rightarrow CO_2 + 2H_2O, \Delta H^0 = -803 \text{ kJ mol}^{-1} \quad (3)$$

### 3–3–4–1. Catalyst preparation

Acetonitrile was used as a solvent for the impregnation method to prepare Ru/$CeO_2$-based catalysts and Pd/$CeO_2$-based catalysts. The solvent in the impregnation procedure is usually water. However, due to their insolubility to water, Ru(acac)$_3$ and Pd(OCOCH$_3$)$_2$ were dissolved in acetonitrile. As a result, 3 wt% Ru/$CeO_2$-based composites and 1 wt% Pd/$CeO_2$-based composites for $CO_2$ methanation and $CH_4$ oxidation, respectively, were obtained.

### 3–3–4–2. Ru/$CeO_2$-based catalysts for $CO_2$ methanation

STEM/EDX and XRF analyses were used to quantify the nanometal contents of the composite catalysts. Fig. 3-8 showed the dispersibility of Ru over the $CeO_2$ supports. Ru was well dispersed over the supports in 3.4–4.5 wt%. XRF analysis also showed 2.1–2.8 wt% Ru contents. A flow-type reactor was selected to conduct $CO_2$ methanation to evaluate the catalytic activity of the composite-supported Ru catalysts. As seen in Fig. 3-9, Ru/$SiO_2$–$CeO_2$-C exhibited a bit better performance than Ru/$CeO_2$-M, Ru/$ZrO_2$–$CeO_2$-C, Ru/$Al_2O_3$–$CeO_2$-C, Ru/$Y_2O_3$–$CeO_2$-C, and $CeO_2$-J.

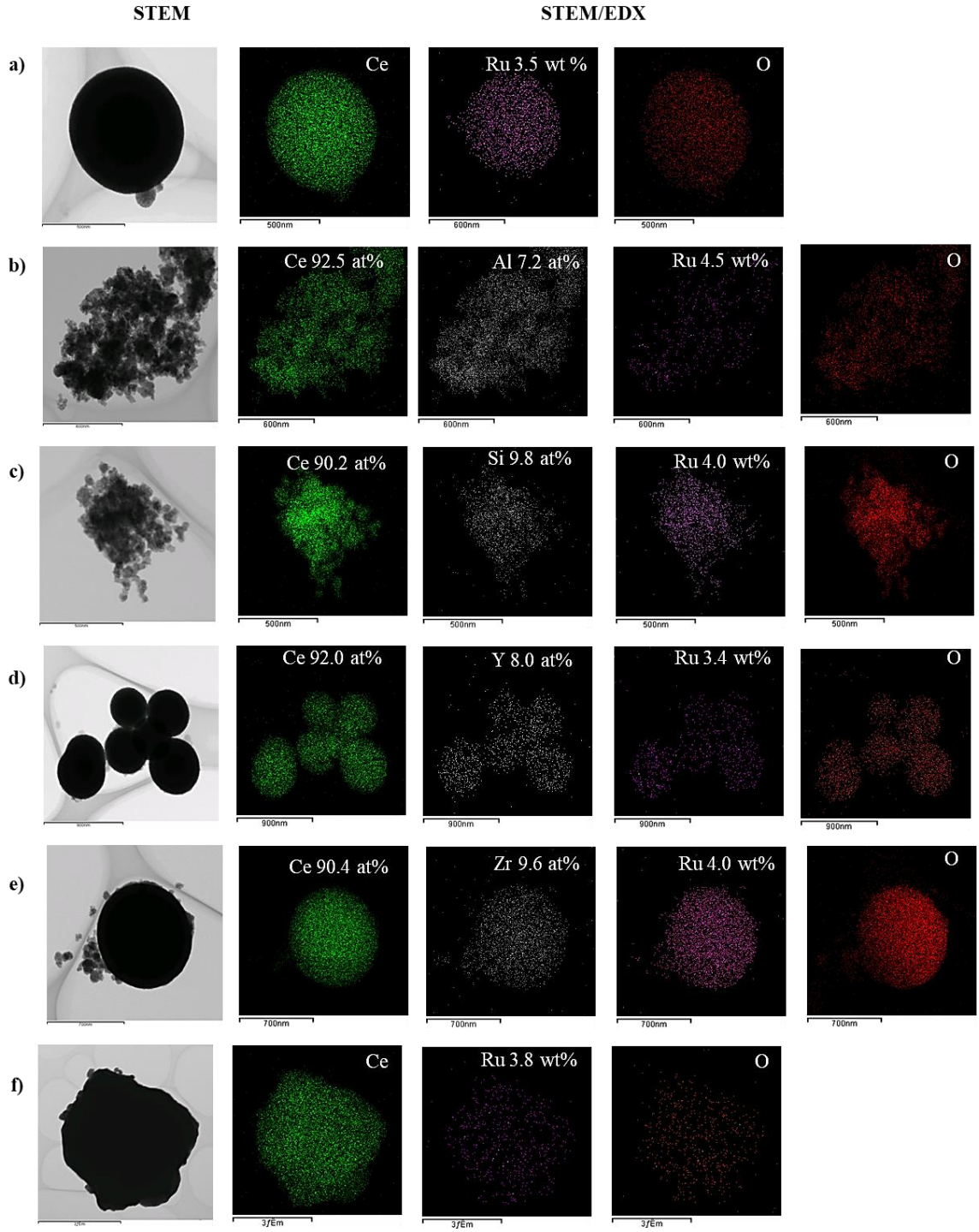


**Fig. 3-8.** STEM/EDX mappings of Ru/$CeO_2$-based catalysts. **a)** Ru/$CeO_2$-M, **b)** Ru/$Al_2O_3$-$CeO_2$-C, **c)** Ru/$SiO_2$-$CeO_2$-C, **d)** Ru/$Y_2O_3$-$CeO_2$-C, **e)** Ru/$ZrO_2$-$CeO_2$-C, and **f)** Ru/$CeO_2$-J.

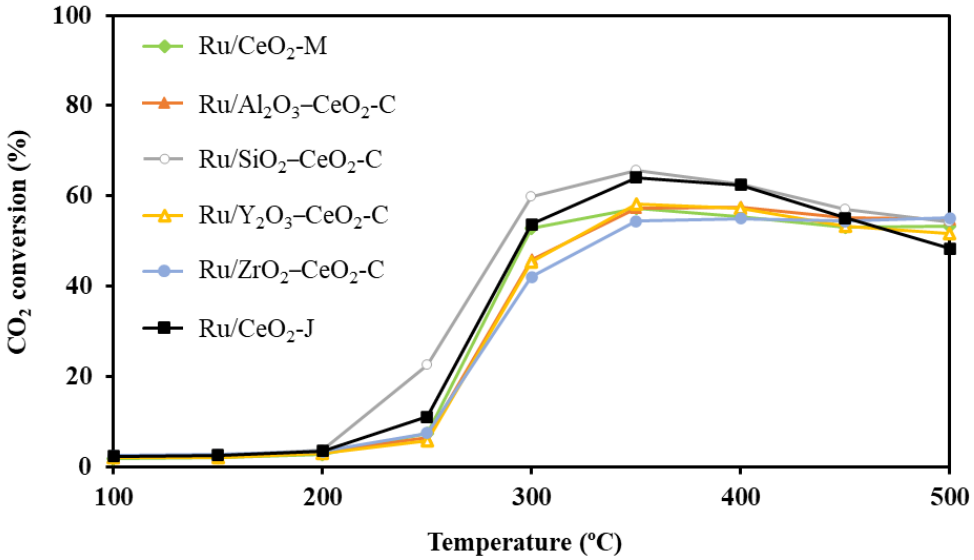


**Fig. 3-9.** $CO_2$ conversion vs. temperature for $CO_2$ methanation over Ru/$CeO_2$-based catalysts.

### 3–3–4–3. Pd/$CeO_2$-based catalysts for $CH_4$ oxidation

For their application in oxidation processes, the higher OSCs obtained through the $Ce^{3+}/Ce^{4+}$ redox shift in $CeO_2$ catalysts and/or catalytic supports are crucial [23]. From prior studies, $CeO_2$ has a greater catalytic capacity for the liquid-phase oxidation of benzyl alcohol and the vapor-phase oxidation of CO as well [18]. Additionally, Pt/$CeO_2$ catalyst exhibited remarkable activity for CO oxidation in the vapor phase. Then, Pd catalysts supported on $CeO_2$-based composites were prepared by an impregnation method and their catalytic activities were investigated. In this study, $CH_4$ oxidation as a specific

reaction was selected, where the oxygen storage and transfer capabilities of the $CeO_2$-based supports are crucial to the reaction.

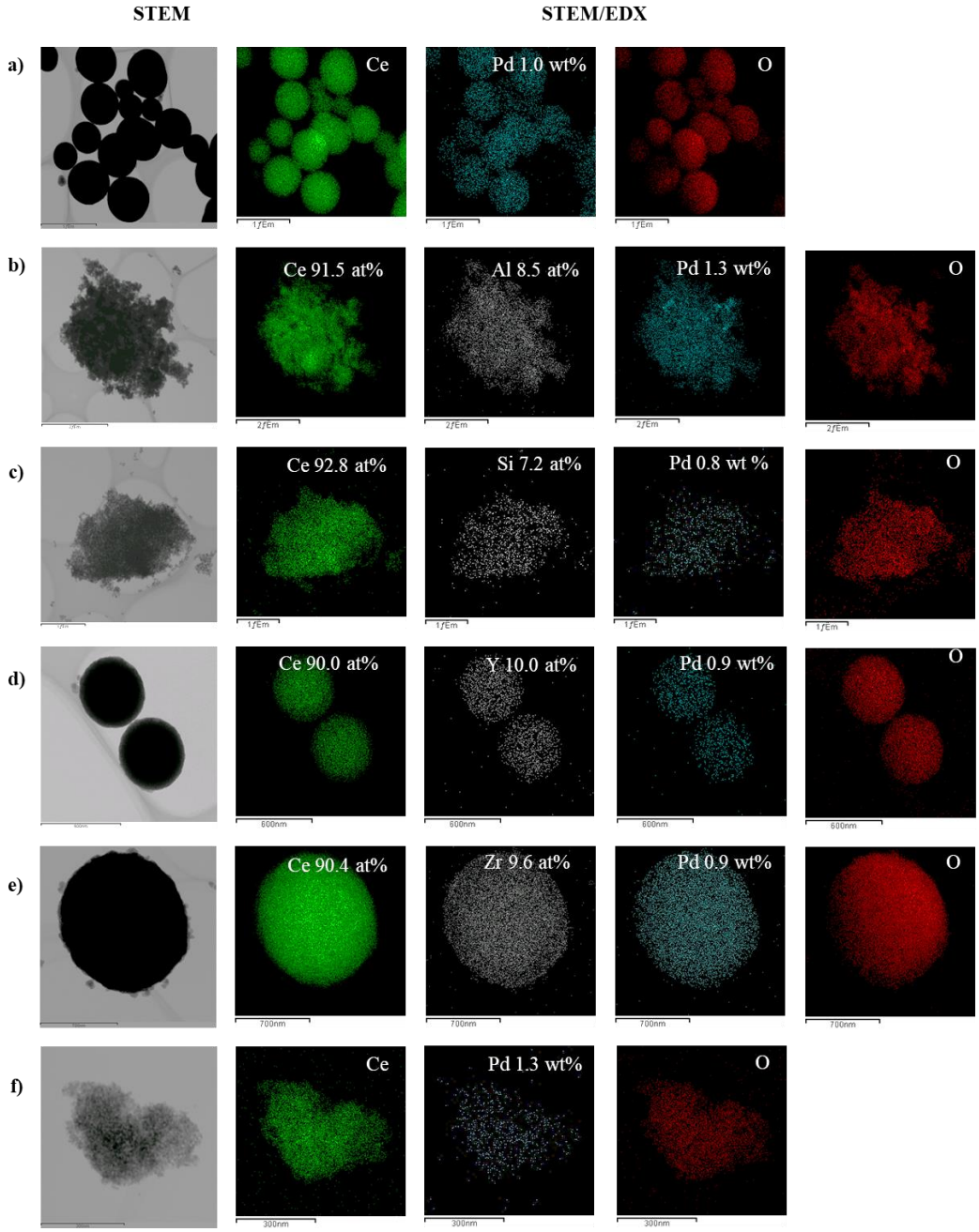


**Fig. 3-10.** STEM/EDX mappings of $Pd/CeO_2$ MARIMO based catalysts. **a)** $Pd/CeO_2$-M, **b)** $Pd/Al_2O_3$-$CeO_2$-C, **c)** $Pd/SiO_2$-$CeO_2$-C, **d)** $Pd/Y_2O_3$-$CeO_2$-C, **e)** $Pd/ZrO_2$-$CeO_2$-C, and **f)** $Pd/CeO_2$-C.

As illustrated in Fig. 3-11, Pd/$CeO_2$ showed catalytic activity at about 400–450 °C. However, the catalytic activity gradually decreased and was lost at temperatures above 500 °C. The $CH_4$ conversion of the Pd catalyst supported on the reference $CeO_2$ catalyst (Pd/$CeO_2$-J) is higher than 90% at 500 °C, which is superior to Pd/$CeO_2$-M. On the other hand, Pd catalysts supported on $CeO_2$-based composites exhibited better low-temperature activities compared to the reference catalyst. Particularly, Pd/$SiO_2$–$CeO_2$-C showed the highest catalytic activity, of which reaction starting at a relatively low temperature of 250 °C and reaching 80% at 300 °C. Thus, the high-performance of the catalyst Pd/$SiO_2$–$CeO_2$-C in $CH_4$ oxidation was successfully prepared by nitrilethermal synthesis and Pd impregnation.

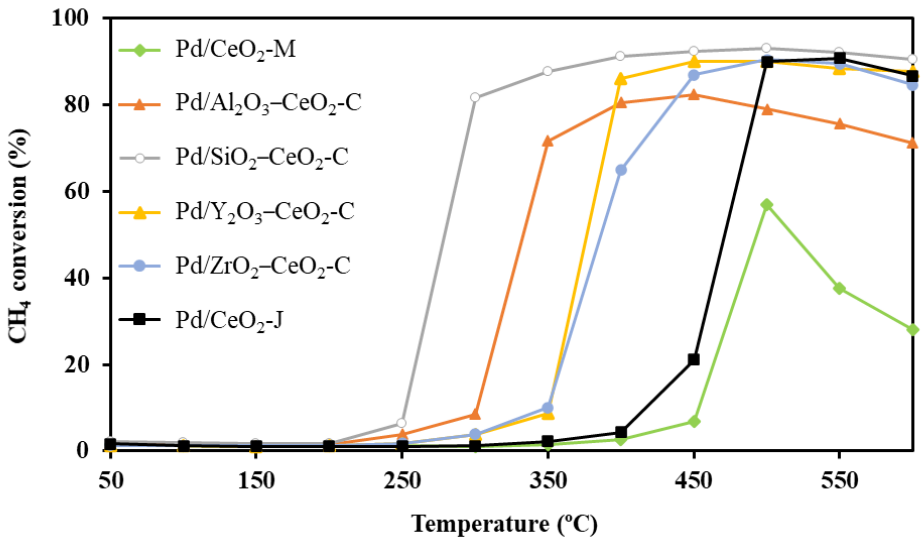


**Fig. 3-11.** $CH_4$ conversion vs. temperature for $CH_4$ oxidation over Pd/$CeO_2$-based catalysts.

## 3–4. Conclusions

A new nitrilethermal synthesis method was developed to obtain $CeO_2$ and $CeO_2$ composites such as, $ZrO_2$–$CeO_2$, $SiO_2$–$CeO_2$, $Al_2O_3$–$ZrO_2$, and $Y_2O_3$–$CeO_2$. Acetonitrile was employed as the solvent for the solvothermal reaction. All the produced composites had high amounts of $Ce^{3+}$ species in the Ce $O_2$ particles and high OSC numbers of over 160 mol-O/g, especially those of $SiO_2$–$CeO_2$-C and $Al_2O_3$–$ZrO_2$-C were more than 430 mol-O/g. Pd catalysts supported on $CeO_2$-based composites, Pd/$SiO_2$–$CeO_2$-C and Pd/$Al_2O_3$–$ZrO_2$-C, showed improved low-temperature catalytic activity for $CH_4$ oxidation.

## References


[1] J. Li, Q. Wu, J. Wu, Synthesis of nanoparticles via solvothermal and hydrothermal methods, in: M. Aliofkhazraei, Handbook of Nanoparticles, Springer Cham., Edinburg, 2015, 1-28.

[2] A. Yoko, G. Seong, T. Tomai, T. Adschiri, Continuous flow synthesis of nanoparticles using supercritical water: process design, surface control, and nanohybrid materials, KONA Powder Part. J., 37 (2020) 28–41, https://doi.org/10.14356/kona.2020002.

[3] T. Adschiri, S. Takami, M. Umetsu, S. Ohara, T. Naka, K. Minami, D. Hojo, T. Togashi, T. Arita, M. Taguchi, M. Itoh, N. Aoki, G. Seong, T. Tomai, A. Yoko, Supercritical hydrothermal reactions for material synthesis, Bull. Chem. Soc. Jpn., 96 (2023) 133–147, https://doi.org/10.1246/bcsj.20220295.

[4] M. Niederberger, Nonaqueous sol–gel routes to metal oxide nanoparticles, Acc. Chem. Res., 40 (2007) 793–800, https://doi.org/10.1021/ar600035e.

[5] C. Aymonier, G. Philippot, A. Erriguible, S. Marre, Playing with chemistry in supercritical solvents and the associated technologies for advanced materials by design, J. Supercrit. Fluids, 134 (2018), 184–196, https://doi.org/10.1016/j.supflu.2017.12.021.

[6] Y. Boyjoo, M. Wang, W.K. Pareek, J. Liu, M. Jaroniec, Synthesis and applications of porous non-silica metal oxide submicrospheres, Chem. Soc. Rev., 45 (2016) 6013–6047, https://doi.org/10.1039/C6CS00060F.

[7] P. Wang, K. Kobiro, Ultimately simple one-pot synthesis of spherical mesoporous $TiO_2$ nanoparticles in supercritical methanol, Chem. Lett., 41 (2012) 264–266, https://doi.org/10.1246/cl.2012.264.

[8] P. Wang, K. Kobiro, Synthetic versatility of nanoparticles: a new, rapid, one-pot, single-step synthetic approach to spherical mesoporous (metal) oxide nanoparticles using supercritical alcohols, Pure Appl. Chem., 86:5 (2014) 785-800, https://doi.org/10.1515/pac-2013–1117.

[9] F. Duriyasart, A. Irizawa, K. Hayashi, M. Ohtani, K. Kobiro, sintering-resistant metal catalysts supported on concave-convex surface of $TiO_2$ nanoparticle assemblies, ChemCatChem, 10 (2018) 3392, https://doi.org/10.1002/cctc.201800624.

[10] E.K.C. Pradeep, M. Ohtani, K. Kobiro, A simple synthetic approach to $Al_2O_3$–$TiO_2$ and ZnO–$TiO_2$ mesoporous hollow composite assemblies consisting of homogeneously mixed primary particles at the nano level, Eur. J. Inorg. Chem., 34 (2015) 5621–5627, https://doi.org/10.1002/ejic.201500964.

[11] M. Meiliefiana, T. Nakayashiki, E. Yamamoto, K. Hayashi, M. Ohtani, K. Kobiro, One-step solvothermal synthesis of Ni nanoparticle catalysts embedded in $ZrO_2$ porous spheres to suppress carbon deposition in low-temperature dry reforming of methane, Nanoscale Res. Lett., 17 (2022), https://doi.org/10.1186/s11671-022-03683-7.

[12] Y. Kumabe, H. Taga, K. Kan, M. Ohtani, K. Kobiro, Porous niobia spheres with large surface area: alcothermal synthesis and controlling of their composition and phase transition behavior, RSC Adv., 10 (2020) 14630–14636, https://doi.org/10.1039/D0RA01704C.

[13] Y. Tanaka, H. Usui, Y. Domi, M. Ohtani, K. Kobiro, H. Sakaguchi, Mesoporous spherical aggregates consisted of Nb-doped anatase $TiO_2$ nanoparticles for Li and

Na storage material, ACS Appl. Energy Mater., 2 (2019) 636–643, https://doi.org/ 10.1021/acsaem.8b01656.

[14] E.K.C. Pradeep, M. Ohtani, T. Kawaharamura, K. Kobiro, Single-step simple solvothermal synthetic approach to ultrafine MgO nanocrystals using high-temperature and high-pressure acetonitrile, Chem. Lett., 46 (2017) 940–943, https://doi.org/10.1246/cl.170185.

[15] B.H. Hoff, Acetonitrile as a building block and reactant, Synthesis, 50 (2018) 2824–2852, https://doi.org/ 10.1055/s-0036-1589535.

[16] J. Buha, I. Djerdj, M. Niederberger, Nonaqueous synthesis of nanocrystalline indium oxide and zinc oxide in the oxygen-free solvent acetonitrile, Cryst. Growth Des., 7 (2007). 113-116, https://doi.org/10.1021/cg060623+.

[17] S. Leubner, R. Stäglich, J. Franke, J. Jacobsen, J. Gosch, R. Siegel, H. Reinsch, G. Maurin, J. Senker, G. Yot, N. Stock, Solvent impact on the properties of benchmark metal–organic frameworks: acetonitrile-based synthesis of CAU-10, Ce-UiO-66, and Al-MIL-53, Chem. Eur. J., 26 (2020) 3877, https://doi.org/10.1002/chem.201905376.

[18] A. Taniguchi, Y. Kumabe, K. Kan, M. Ohtani, K. Kobiro, $Ce^{3+}$-enriched spherical porous ceria with an enhanced oxygen storage capacity, RSC Adv., 11 **(**2021) 5609–5617, https://doi.org/10.1039/D0RA10186A.

[19] J.R.A. Sietsma, A.J. Van Dillen, P.E. De Jongh, K.P. De Jong, Application of ordered mesoporous materials as model supports to study catalyst preparation by impregnation and drying, Stud. Surf. Sci. Catal., 162 (2006) 95–102, https://doi.org/10.1016/S0167-2991(06)80895-5.

[20] Z. Niu, Y. Li, Removal and utilization of capping agents in nanocatalysis, Chem Mater, 26 (2014) 72–83, https://doi.org/10.1021/cm4022479.

[21] J. Kammert, J. Moon, Z. Wu, A review of the interactions between ceria and $H_2$ and the applications to selective hydrogenation of alkynes, Chin. J. Catal., 41 (2020) 901–914, https://doi.org/10.1016/S1872-2067(19)63509-6.

[22] S. Song, X. Wang, H. Zhang, $CeO_2$-encapsulated noble metal nanocatalysts: enhanced activity and stability for catalytic application, NPG Asia Mater 7, (2015), https://doi.org/10.1038/am.2015.27.

[23] X. Courtois, N. Bion, P. Marécot, D. Duprez, The role of cerium-based oxides used as oxygen storage materials, in $DeNO_x$ catalysis, in: P. Granger, V.I. Pârvulescu, Studies in surface science and catalyst, Elsevier, Amsterdam, 2007, 235–259.

## Conclusions

One-pot single-step solvothermal synthetic method of porous metal oxides with controlled morphologies and attractive properties has been develop by changing the role of solvent. Ni nanoparticles supported in $ZrO_2$ porous spheres and $ZrO_2$ composites were successfully prepared through a one-pot single-step alcothermal reaction. Ni NP catalysts in smaller $ZrO_2$ porous spheres and $ZrO_2$ composite spheres featured high heat resistance properties and high specific surface areas up to 196 $m^2/g$. In their applications, Ni nanoparticles embedded in $SiO_2$–$ZrO_2$-C showed the excellent catalytic activity and stability with a small amount of carbon deposition during the dry reforming of methane (DRM) at 550 °C for 15 h.

On the other hand, a one-pot and one-step solvothermal reaction in acetonitrile, termed 'nitrilethermal' synthesis, was successfully developed to obtain $CeO_2$ and $CeO_2$-based composites. Homogeneously mixed composite oxides showed a high specific surface area of 101–152 $m^2/g$. The composites showed high oxygen storage capacities exceeding 500 μmol-O/g. Afterwards, these composites were used as the supports for nanometal Ru and Pd catalysts for $CO_2$ methanation and $CH_4$ oxidation, respectively. Ru/$SiO_2$–$CeO_2$ demonstrated a slightly higher activity for $CO_2$ methanation, while Pd/$SiO_2$–$CeO_2$-C and Pd/$Al_2O_3$–$CeO_2$-C demonstrated superior low-temperature activities for $CH_4$ oxidation.

Thus, this thesis proved the usefulness and versatility of alcothermal and nitrilethermal synthesis producing metal oxide porous spheres as catalyst supports.

## List of Publications:

1. M. Meiliefiana, T. Nakayashiki, E. Yamamoto, K. Hayashi, M. Ohtani, K. Kobiro, One-step Solvothermal Synthesis of Ni Nanoparticle Catalysts Embedded in $ZrO_2$ Porous Spheres to Suppress Carbon Deposition in Low-temperature Dry Reforming of Methane, Nanoscale Res. Lett., 17 (2022).
2. M. Meiliefiana, T. Nakayashiki, K. Kobiro, Nitrilethermal synthesis of $CeO_2$-based composite nanoparticles as Ru and Pd catalyst supports for $CO_2$ methanation and $CH_4$ oxidation, J. Supercrit. Fluids, 201 (2023), 106008–106015.

## List of presentations:

1. High Performance of Ni Catalysts Embedded in $ZrO_2$ Porous Spheres Prepared by One-Step Solvothermal Synthesis, *International Solvothermal and Hydrothermal Association 2021 (ISHA 2021)*, Virtual Conferences, Oral presentation 26$^{th}$–28$^{th}$ October 2021.
2. One-Step Solvothermal Synthesis of Ni Catalysts Supported on $ZrO_2$-Based Porous Spheres and Their Catalytic Activity for Dry Reforming of Methane, M. Meiliefiana, T. Nakayashiki, E. Yamamoto, K. Hayashi, M. Ohtani, K. Kobiro, *Japan Chemistry Society Shikoku 2021*, Virtual Conferences, Oral presentation, 13$^{th}$–14$^{th}$ November 2021.
3. Nitrilethermal Synthesis of Pd Catalysts Embedded in $CeO_2$ MARIMO with an Enhanced Oxygen Storage Capacity, M. Meiliefiana, T. Nakayashiki, K. Kobiro, *Kochi Chemical Symposium 2022*, Kochi, Japan, Poster presentation, 29$^{th}$ October 2022.

# Acknowledgement

I am deeply indebted to my supervisor, Professor Kazuya Kobiro, not only for providing me the opportunity to carry on this research in the laboratory, but also for his valuable help, suggestions, and comments during this research and writing this thesis. I would like to be thankful to the current and former members of our lab. Also, I would like to thank my co-supervisors; Professor Nagatoshi Nishiwaki, Professor Masataka Ohtani his kind help, advice, and guidance. Moreover, I would like to thank to Associate Professor Akitaka Ito, and Professor Hisao Makino for the guidance they provided.

I would like to express my sincere gratitude Paul Daniels for teaching of English academic writing and their kind advices. Specially, I would like to thank Special Scholarship Program (SSP) of Kochi University of Technology and Japan Student Services Organization (JASSO) for the scholarships I received for my doctoral studies.

Last, but not least I would like to appreciate the support, understanding, and the patience of my composite and friends. Thank you for sharing memorable time during these three years. Also, thank you for your sympathetic and encouragement. Most of all, I would like to express my deepest gratitude to my family who always pay attention to me all the times.

# APPENDICES

Appendix 1 (Chapter II)

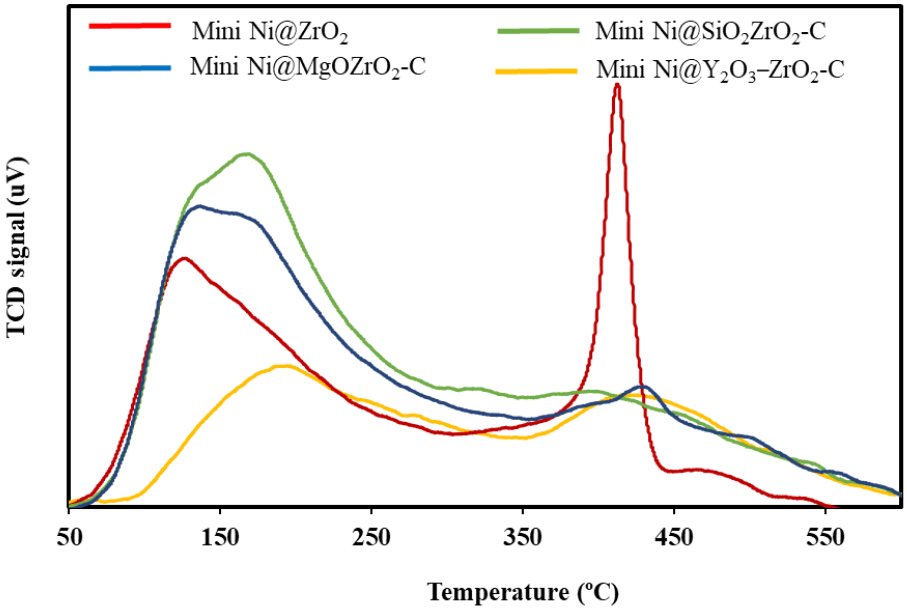


**Fig. A2-1.** $CO_2$-TPD analysis of Mini-series of Ni@$ZrO_2$-based composites.

Appendix 2 (Chapter III)

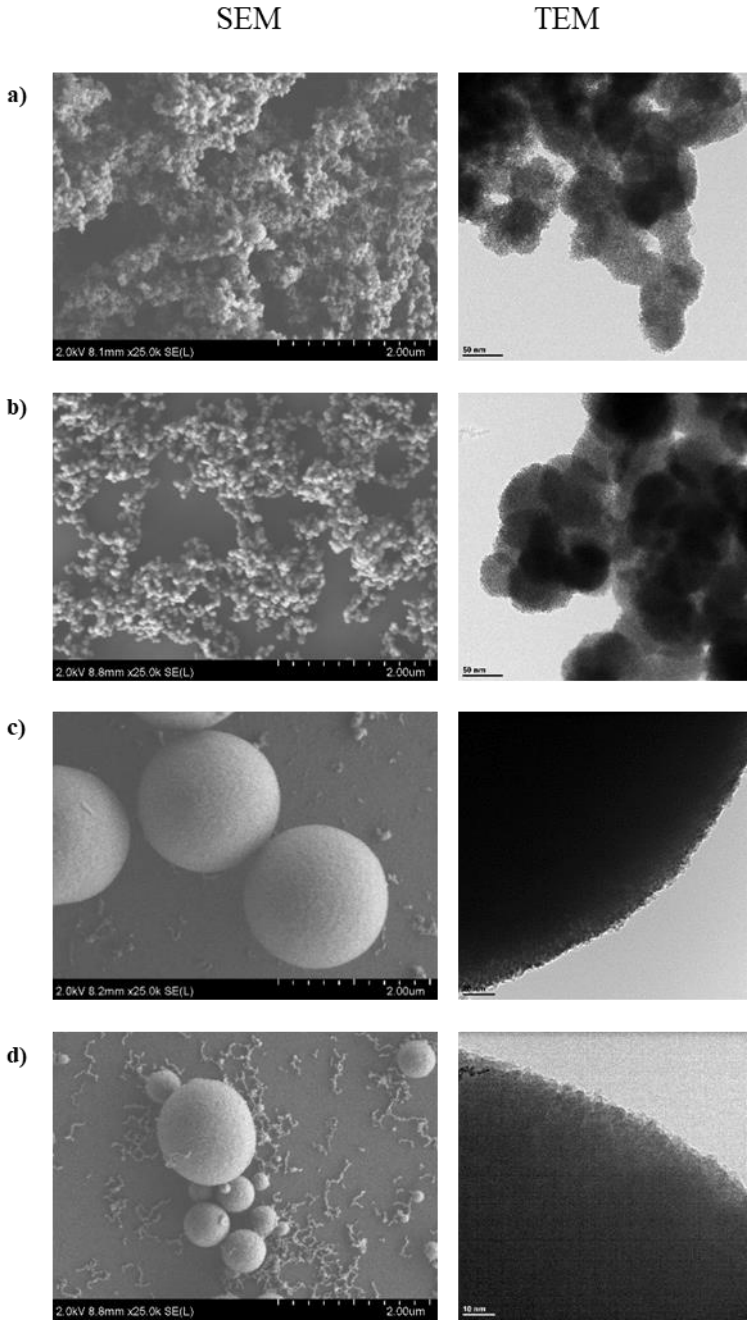


**Fig. A3-1.** SEM and TEM images of Pd@$CeO_2$-based composites. **a)** $ZrO_2$–$CeO_2$-C, **b)** $SiO_2$–$CeO_2$-C, **c)** $Al_2O_3$–$CeO_2$-C, and **d)** $Y_2O_3$–$CeO_2$-C.

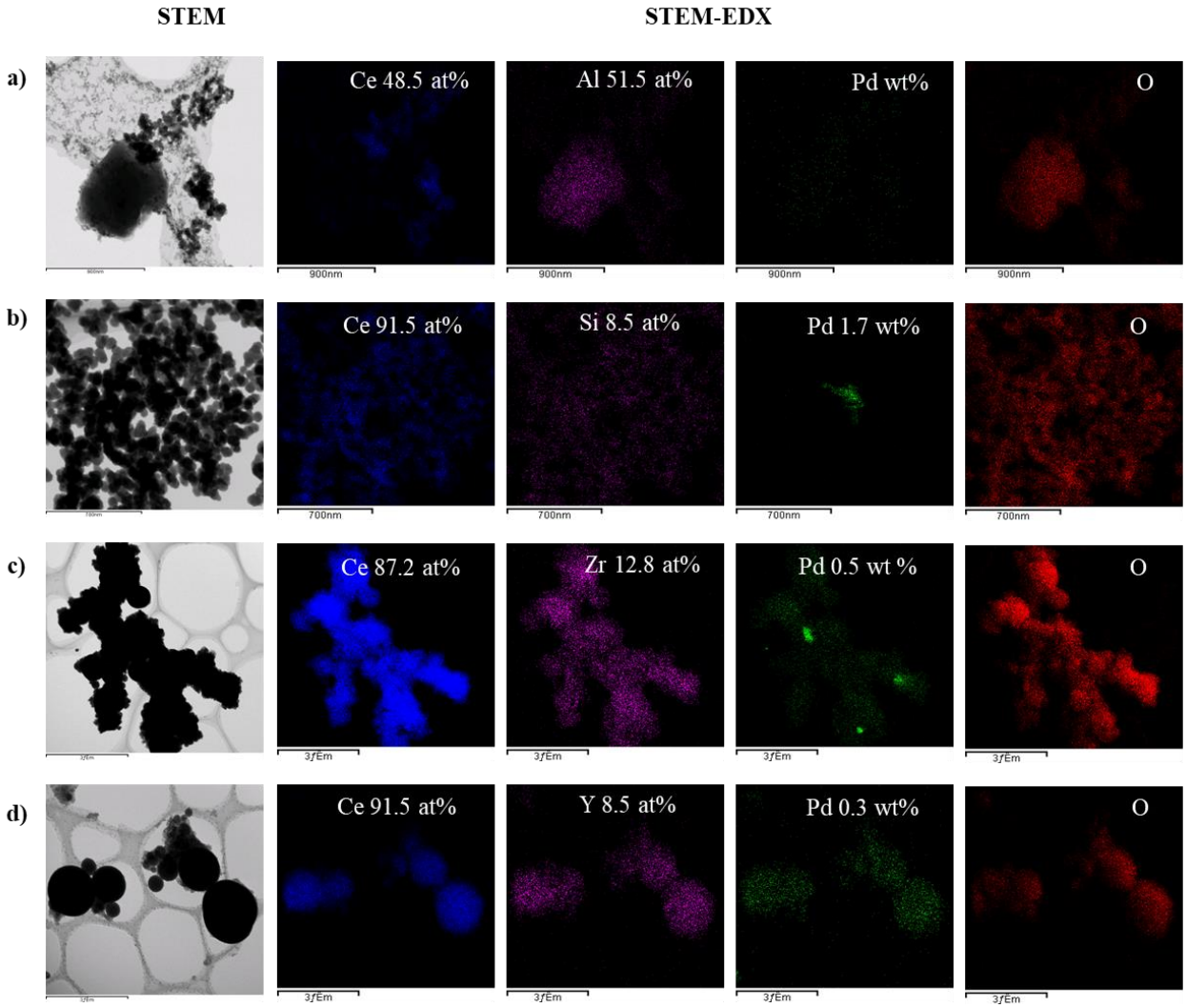


**Fig. A3-2.** STEM/EDX images of Pd@$CeO_2$-based composites. **a)** $ZrO_2$–$CeO_2$-C, **b)** $SiO_2$–$CeO_2$-C, **c)** $Al_2O_3$–$CeO_2$-C, and **d)** $Y_2O_3$–$CeO_2$-C.

Table A3.1

Metal size and dispersibility on $Ru/CeO_2$-based support and reference support

| Materials | Metal dispersion (%) | Metal size (nm) | Specific surface area ($m^2/g$) |
|---|---|---|---|
| $Ru/CeO_2$ | 39.71 | 3.38 | 63 |
| $Ru/Al_2O_3$-$CeO_2$ | 35.94 | 3.73 | 73 |
| $Ru/SiO_2$-$CeO_2$ | 40.33 | 3.33 | 78 |
| $Ru/Y_2O_3$-$CeO_2$ | 34.72 | 3.86 | 71 |
| $Ru/ZrO_2$-$CeO_2$ | 16.66 | 8.06 | 61 |
| $Ru/CeO_2$-JRC | 72.69 | 1.84 | 21 |

Table A3.2 same as before

Metal size and dispersibility on $Pd/CeO_2$-based support and reference support

| Materials | Metal dispersion (%) | Metal size (nm) | Specific surface area ($m^2/g$) |
|---|---|---|---|
| $Pd/CeO_2$ | 70.35 | 1.59 | 33 |
| $Pd/Al_2O_3$-$CeO_2$ | 59.34 | 1.88 | 40 |
| $Pd/SiO_2$-$CeO_2$ | 46.96 | 2.38 | 60 |
| $Pd/Y_2O_3$-$CeO_2$ | 26.63 | 4.19 | 29 |
| $Pd/ZrO_2$-$CeO_2$ | 72.68 | 1.54 | 55 |
| $Pd/CeO_2$-JRC | 72.46 | 1.54 | 48 |